J. Fluid Mech. (1993), *vol.* 254, *pp.* 529–559

On internal waves generated by travelling wind

By **PIJUSH K. KUNDU**

Oceanographic Center, Nova University, Dania, FL 33004, USA

(Received 10 October 1992 and in revised form 22 March 1993)

Oceanic internal waves forced by a latitude-independent wind field travelling eastward at speed U is investigated, extending the hydrostatic f-plane model of Kundu & Thomson (1985). The ocean has a well-mixed surface layer overlying a stratified interior with a depth-dependent buoyancy frequency $N(z)$, and f can vary with latitude. Solutions are found by decomposition into vertical normal modes. Problems discussed are (i) the response to a slowly moving line front, and (ii) the response in a variable-f ocean.

For the slowly moving line front assuming a depth-independent N, the trailing waves are found to have large frequencies, and the vertical acceleration $\partial w/\partial t$ is important (that is the dynamics are non-hydrostatic) if the frequency ω is larger than a few times $(Nf)^{\frac{1}{2}}$. The wake contains waves associated with all vertical modes, in contrast to hydrostatic dynamics in which slowly moving line fronts do not generate trailing waves of low-order modes. It is argued that slowly moving wind fields can provide an explanation for the frequently observed broad peak in the spectrum of vertical motion at a frequency somewhat smaller than N, and of the vertical coherence of the associated waves in the upper ocean.

To study lower-frequency internal waves, the hydrostatic constant-f model of Kundu & Thomson is extended to variable f. Various sections through such a flow clearly illustrate the development of a meridional wavelength $\lambda_y = 2\pi/\beta t$ as predicted by D'Asaro (1989), in addition to the zonal wavelength λ_x due to translation of the wind. The two effects combine to cause a greater horizontal inhomogeneity, so that energy from the surface layer descends quickly, travelling equatorward and downward. Since waves at any point arrive from different latitudes, spectra no longer consist of discrete peaks but are more continuous and broader than those in the constant-f model. The waves are more intermittent because of the larger spectral width, and vertically less correlated in the thermocline because of a larger bandwidth of vertical modes. The vertical correlation in the deep ocean, however, is still high because the response is dominated by one or two low-order modes after 30 days of integration. As U decreases, the larger bandwidth of frequency increases the intermittency, and the larger bandwidth of vertical wavenumber decreases the vertical correlation. A superposition of travelling wind events intensifies the high-frequency end of the spectrum; a month-long travelling series of realistic strength can generate waves with amplitudes of order 4 cm/s in the deep ocean.

It is suggested that propagating winds and linear dynamics are responsible for the generation of a large fraction of internal waves in the ocean at all depths. The main effect of nonlinearity and mean flow may be to shape the internal wave spectra to a ω^{-2} form.

1. Introduction

Internal waves are gravity waves within a stratified fluid. Reviews can be found in Thorpe (1975), Phillips (1979), Garrett & Munk (1979), Munk (1981), Gill (1982), and Olbers (1983). In the atmospheric stratosphere and in the ocean observations indicate that they are as ubiquitous as waves at the surface of the ocean. Compared to surface waves, they have much slower propagation speed and much larger amplitude, the strongest ones moving the surfaces of constant density in the ocean by as much as 100 m vertically. The frequency ω of these waves lies in the range $f < \omega < N$, where f is the Coriolis frequency and N is the buoyancy frequency. The review papers listed above summarize several methods of generation, such as moving pressure fields, resonant interaction of a pair of surface waves, geostrophic adjustment after flow instabilities, and oscillating flow over bottom topography. Away from the equator, both stratospheric (Cornish & Larsen 1989) and oceanic observations indicate that there is a strong peak at a frequency slightly above f. The corresponding motion is generally called an *inertial wave* (or near-inertial wave), while motion exactly at the limiting frequency $\omega = f$ is generally referred to as *inertial oscillation*. In the latter case there is no wave motion, just motion of the fluid particles in horizontal circular orbits.

The generation of oceanic internal waves by a moving wind-stress field is studied here in a linear model, extending the constant-f hydrostatic model of Kundu & Thomson (1985, referred to herein as KT85). Special emphasis is given to the behaviour of the waves near the low-frequency limit f, namely the inertial waves. The present work (i) reviews the relevant observations and models, (ii) examines some consequences of eliminating the hydrostatic assumption in a constant-f model, and (iii) studies the effects of latitudinal variation of f in a hydrostatic model. It will be seen that the travelling winds can provide an explanation for several observed features of internal waves in the ocean.

The notation is defined here to facilitate further discussion. The spatial coordinates (x, y, z) and the velocity components (u, v, w) are in the (eastward, northward, upward) directions, $R_e (= 6371 \text{ km})$ is the radius and $\Omega (= 2\pi \text{ day}^{-1})$ is the angular velocity of the earth, θ is the latitude, and $\beta \equiv \mathrm{d}f/\mathrm{d}y = 2\Omega \cos\theta / R_e$ is the latitudinal variation of f.

2. Some observed characteristics of inertial waves

A good review of inertial waves is given in Fu (1981). Some of the observed characteristics are listed below.

(i) After a storm the velocity in the surface layer can reach values as high as 70 cm/s (Thomson & Huggett 1981). Below the thermocline amplitudes decrease with depth, reaching 3–4 cm/s near ocean bottom (Sanford 1975).

(ii) They are observed nearly everywhere, except very close to the equator. Recent observations do not indicate that 'they are particularly pronounced at the latitudes where f coincides with one of the tidal frequencies' (Phillips 1977, p. 243).

(iii) The motion is intermittent, and can persist anywhere from about 3–4 periods (Kundu 1976) to 20 periods (Thomson & Huggett 1981). Short persistence means that the bandwidth $\Delta\omega$ of the inertial peak is wide, with $f/\Delta\omega \approx 10$ if the persistence time is 10 inertial periods.

(iv) Horizontal coherence scale Δx has been reported to vary over a wide range, from a few kilometres (Kundu 1976) to 50 km (Fu 1981; Paduan, de Szoeke & Weller

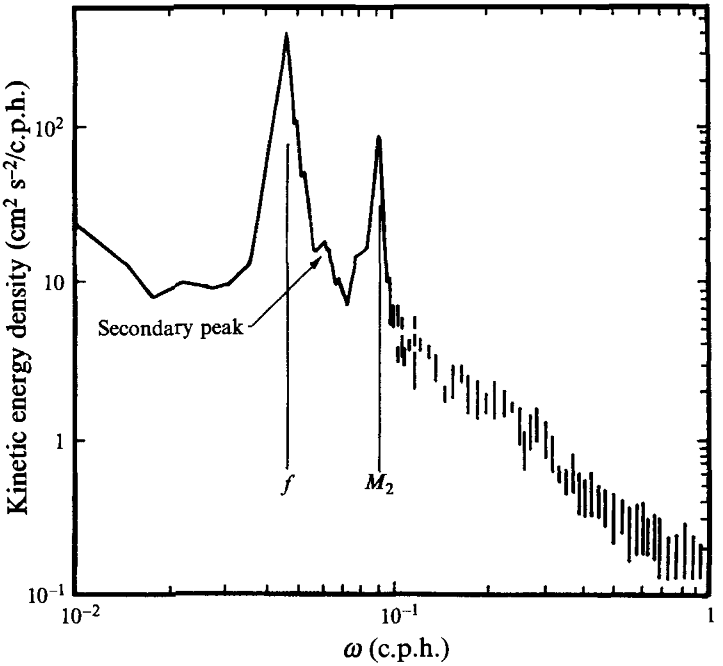

FIGURE 1. Frequency spectrum of horizontal velocity variance, measured in the western Atlantic ocean by Gould, Schmitz & Wunch (1974). Average of spectra at depths of 1503 m and 1522 m is shown, because the individual spectra at these two depths were not labelled. Note the secondary peaks to the right of the inertial peak.

1989) to nearly 500 km (Thomson & Huggett 1981). Low coherence scale signifies that the horizontal wavenumber bandwidth of the inertial waves is large, since $\Delta k \sim 1/\Delta x$.

(v) Vertical coherence scales have been reported to be about 100 m in the upper thermocline, about 200 m in the lower thermocline, and larger than 1000 m in the deep ocean with little phase change (Fu 1981). Therefore the vertical structure in the deep ocean frequently appears as standing waves, indicating the dominance of one or two low-order modes.

(vi) Repeated vertical profiles have frequently revealed a dominant downward energy propagation (Sanford 1975; Kunze & Sanford 1986), except near rugged bottom topography where upward energy propagation has also been detected (Kunze & Sanford 1986).

(vii) The inertial peak is generally observed at a frequency slightly larger than f. This 'blue-shift' of the inertial peak is found to increase with depth (Fu 1981).

(viii) The inertial peak is not only broad, it also frequently contains a stepped structure, especially on the high-frequency side. Moreover, secondary peaks are frequently observed at a frequency somewhat larger than f (figure 1). We shall come back to this point when we discuss the model results.

3. Review of earlier models

At least three kinds of theories have been proposed for the generation of inertial waves in the ocean interior, namely *wave–wave interaction*, *remote* (or '*global*') *generation* and *local generation*. Wave–wave interaction involves a triad of internal waves that can transfer energy among themselves through the nonlinear interaction terms in the equations of motion. Calculations of McComas & Bretherton (1977) show that one variant of this mechanism, called *subharmonic instability*, is particularly effective in transferring energy from higher frequency waves to inertial waves.

Remote generation theory was first proposed by Munk & Phillips (1968), and followed up by Munk (1980) and Fu (1981). The idea is that high-frequency internal waves randomly generated at lower latitudes can travel poleward to their turning latitude where their frequency equals the local Coriolis frequency (that is, $\omega = f$), and reflect backward. Near the turning latitude the latitudinal structure of the horizontal velocity is proportional to the Airy function, which is oscillatory equatorward of the turning latitude and exponentially decaying poleward of it. The Airy function reaches its maximum magnitude slightly equatorward of the turning latitude, where the constructive interference of the different Airy functions corresponding to different vertical modes form a single peak. This leads to a horizontal velocity spectrum in which the peak occurs at a frequency slightly larger than the local f. The global generation model is vertically isotropic, that is there is no net vertical flux of energy. It would seem, therefore, that the observed dominance of downward energy (upward phase) propagation of inertial waves is direct evidence that most of the inertial energy in the thermocline and above is locally generated near the surface. However, the theory may have some validity in the deep ocean.

Apart from the works mentioned in the preceding paragraph, most other studies have attempted to explain the generation of inertial waves by wind forcing at the surface. Assuming f to be constant, Pollard (1970) studied the geostrophic adjustment after sudden application of a horizontally bounded wind, concluding that much of the inertial waves in the upper ocean is due to wind forcing. However, in the deep ocean the inertial waves in Pollard's solution sharply decreased to negligible values, leading him to conclude that inertial waves in the deep ocean are either generated by the action of several storms at the surface, or they are due to other effects such as remote generation, not present in his constant-f model.

There is now considerable evidence indicating that propagating atmospheric disturbances are a very potent source of inertial waves in the upper ocean (Thomson & Huggett 1981; D'Asaro 1985). Aspects of this phenomenon have been studied in several models. Geisler (1970) developed a two-layer, hydrostatic, constant-f model of the response to a spatially limited region of wind-curl moving zonally at uniform speed U, and showed that the nature of the solution depends on the magnitude of U relative to the eigenspeed c_n of the modes. For common oceanographic parameter values the baroclinic modes satisfy $U > c_n$, for which the equation of motion is hyperbolic and the solution has a laterally spreading wake in which the response decays with downstream distance approximately as $x^{\frac{1}{2}}$. The barotropic mode usually satisfies $U < c_n$, for which the system is elliptic and gives a symmetric response with no wake. He also showed that travelling atmospheric *pressure fluctuations* are far less efficient in generating internal waves than a travelling wind-curl region. Greatbatch (1983, 1984) discussed the effects of nonlinearity, mixing and various scales on a similar problem.

The variation of f with latitude is obviously quite important for inertial waves, because they are near their turning latitude and cannot propagate far poleward. Geisler & Dickinson (1972) extended the constant-f calculation of Geisler (1970) to variable f, using only a single mode. Results showed that the response at a given point is first dominated by waves coming directly from the source, and then by waves reflected from turning points poleward of the source. Anderson & Gill (1979) studied the effect of β on the horizontal propagation of a single vertical mode excited by a suddenly imposed wind confined between two latitudes, and concluded that some of the superinertial ($\omega > f$) energy found at a lower latitude is in fact due to the dispersion of inertial energy generated at higher latitudes. Price (1983) studied the nonlinear response due to a moving hurricane in a five-layer numerical model, and found a rapid outward and downward spreading of energy from the forced area at the surface. In an insightful paper, Gill (1984) studied the geostrophic adjustment of an x-independent zonal current in the surface layer; such a current would be generated instantly in the wake of a storm propagating infinitely fast. He showed that the initial loss of energy from the mixed layer is sufficient to provide a major source of energy for internal waves below the mixed layer. He also found that the magnitude is intermittent, horizontal and vertical scales tend to decrease with time, and there is some bottom intensification of energy.

The variation of f not only results in the equatorward turning of the inertial waves, it also introduces the horizontal inhomogeneity necessary for the leakage of energy from the surface layer. D'Asaro (1989) demonstrated this feature in the following simple way. Let $f \approx f_0 + \beta y$, where f_0 is the value of f in the middle of the region of interest. Sudden application of a horizontally uniform wind will immediately start local inertial oscillations ($\omega = f$) in the surface mixed layer, of the form $u + \mathrm{i}v = \tilde{U}\exp(-\mathrm{i}ft)$, where $\tilde{U}$ is the complex amplitude. The variation of frequency with y results in meridional phase difference, and the motion becomes inertial waves of the form

$$u + \mathrm{i}v = \tilde{U}\,\mathrm{e}^{-\mathrm{i}ft} = \tilde{U}\,\mathrm{e}^{-\mathrm{i}f_0 t - \mathrm{i}\beta y t}$$

which has a locally constant frequency f_0, and a *southward wavenumber* βt which increases with time, producing an ever-decreasing meridional wavelength

$$\lambda_y = 2\pi/\beta t. \tag{1}$$

Therefore, the motion will always develop horizontal scales small enough to leak energy efficiently from the mixed layer to the thermocline. D'Asaro concentrated on the decay times of inertial motion in the surface layer, and estimated an upper limit of 1–2 weeks. He did not examine the flow below.

Recently Eriksen (1993) studied the response to a zonal band of wind travelling eastward over the equator at $U = 1000$ cm/s. He showed that 20 vertical modes of the gravity and Yanai waves sum to produce oscillations near the local f surprisingly close ($\sim 2°$) to the equator, analogous to the mid-latitude inertial waves studied here. His explanation of the spectral peaks in sea-level data from the tropical Pacific as being generated by travelling wind seems more plausible than the zero-group-velocity argument given by Wunch & Gill (1976).

4. Discussion of constant-f calculations

Many of the works cited in the preceding pages did not examine the characteristics of spectra, coherence, and intermittency of their model inertial waves, or of the flow below the surface layer. Yet these are some of the intriguing features of inertial motion. KT85 developed a two-dimensional hydrostatic model to study these features of inertial waves forced by a propagating front, treating f as constant. Eriksen (1988*a*) compared some results of this model to the near-inertial part of the frequency spectra measured at several depths in the upper 300 m in the Sargasso sea, and concluded that the vertical distribution of the measured spectra can be explained as the response to random translating wind systems. In another work, Eriksen (1988*b*) found close correspondence between the vertical wavenumber spectra predicted by KT85 and the observed spectra synthesized by Garrett & Munk (1979).

A summary of the governing equations from KT85, plus a discussion of their solution, are given in this section. Many of the equations and ideas provided here are used in the next section, which discusses the solution of the same problem for variable f. Some features of the model not brought out in KT85 are pointed out, and consequences of including the vertical acceleration w_t in the equations of motion are discussed.

4.1. *Governing equations*

Consider a continuously stratified ocean of buoyancy frequency $N(z)$, with a surface mixed layer of thickness h in which $N = 0$ and a flat bottom at $z = -D$. The ocean is forced by a y-independent wind stress (τ^x, τ^y) assumed to propagate eastward at uniform speed U. Let p be the perturbation pressure (that is, the pressure difference from the initial state of no motion), and ρ the perturbation density. Since f is regarded as constant, the problem is y-independent. Then the Boussinesq equations of motion under the hydrostatic, inviscid, and linear approximations are

$$u_t - fv = -p_x + F, \quad v_t + fu = G, \quad u_x + w_z = 0, \quad \rho_t - N^2 w/g = 0, \quad p_z + \rho g = 0, \tag{2a–e}$$

where subscripts denote derivatives. The stress is assumed to enter the ocean as a body force in a surface mixed layer of thickness h. Consequently

$$(F, G) = (\tau^x/h, \tau^y/h)$$

in the surface layer, and zero below.

The rigid-lid boundary conditions, which hold for all baroclinic modes, are

$$w = 0 \quad \text{at} \quad z = 0, -D. \tag{3}$$

Solutions to (2), subject to (3), can be found by expanding the variables in terms of the vertical normal modes $\Psi_n(z)$ of the system:

$$(u, v, p) = \sum_{n=0}^{\infty} (u_n, v_n, p_n)\, \Psi_n, \quad w = \sum_{n=0}^{\infty} w_n \int_{-D}^{z} \Psi_n \,\mathrm{d}z, \quad \rho = \sum_{n=0}^{\infty} \rho_n \Psi_{nz}, \tag{4}$$

where $n = 0$ is the barotropic mode, and $n \geqslant 1$ are the baroclinic modes. The eigenfunctions satisfy

$$\left(\frac{\Psi_{nz}}{N^2}\right)_z + \frac{1}{c_n^2}\Psi_n = 0, \quad \text{with} \quad \Psi_{nz} = 0 \quad \text{at} \quad z = 0, -D. \tag{5}$$

Since the magnitude of an eigenfunction is arbitrary, the convenient normalization $\Psi_n(0) = 1$ is adopted for all modes. Substituting (4) into (2) and eliminating ρ_n and w_n, the equations governing the modal coefficients are

$$u_{nt} - fv_n + p_{nx} = \tau_n^x, \quad v_{nt} + fu_n = \tau_n^y, \quad p_{nt} + c_n^2 u_{nx} = 0, \tag{6a–c}$$

where the forcing coefficients are given by

$$(\tau_n^x, \tau_n^y) \equiv (\tau^x, \tau^y) \Big/ \int_{-D}^{z} \Psi_n^2 \,\mathrm{d}z. \tag{7}$$

It can be shown that τ_n is the projection of a step function of magnitude τ in the surface mixed layer on mode n. A good discussion of the technique of normal mode decomposition, including allowance for damping, is given in McCreary (1981).

The equation for u_n alone obtained from (6) is

$$(\partial_{tt}+f^2)\,u_n - c_n^2\,u_{nxx} = \tau^x_{nt}+f\tau^y_n. \tag{8}$$

The forced solution is steady in the moving coordinate

$$\xi \equiv x-Ut \tag{9}$$

fixed with the wind, the transformations $\partial_t \to -U\partial_\xi$ and $\partial_x \to \partial_\xi$ relating the fixed and moving coordinates. Assume that the forcing term in (8) has the form

$$\tau^x_{nt}+f\tau^y_n = U\bar{\tau}_n\,\delta(\xi) \to \tau^x_t+f\tau^y = U\bar{\tau}\,\delta(\xi), \tag{10}$$

where $\delta(\xi)$ is the delta function, and $\bar{\tau}_n$ is the projection of $\bar{\tau}$ on mode n, as in (7). In the absence of τ^y, equation (10) becomes $\tau^x_\xi = -\bar{\tau}\delta(\xi)$. This signifies that τ^x undergoes a sudden spatial drop of $\bar{\tau}$ in moving coordinates, or a sudden temporal increase of $\bar{\tau}$ in fixed coordinates. The forcing then represents a *line front* independent of y. In the presence of both τ^x and τ^y the forcing (10) does not have such a simple physical interpretation, and the solution to (3) then simply represents the 'impulse response' or Green's function.

Let u^δ_n be the impulse response for mode n. In terms of the moving coordinate, (8) becomes

$$u^\delta_{n\xi\xi}+k_n^2\,u^\delta_n = \frac{U\bar{\tau}_n\,\delta(\xi)}{U^2-c_n^2}, \tag{11}$$

where

$$k_n \equiv \frac{f/U}{(1-c_n^2/U^2)^{\frac{1}{2}}} \tag{12}$$

represents the wavenumber. For common oceanographic parameters, typical values are $c_0 \sim 20000$ cm/s, $c_1 \sim 250$ cm/s, and $U \sim 100$–200 cm/s. The barotropic mode almost certainly satisfies $U < c_0$, for which the solution of (11) is symmetric and decays exponentially away from the front. The baroclinic modes generally satisfy $U > c_n$, for which (11) has a trigonometric solution confined in the wake of the front. (Section 4.5 will show that in a non-hydrostatic model internal waves of all modes exist in the wake, whatever the relative values of U and c_n, as long as $\omega > N$.) Unless otherwise stated, all baroclinic modes will be assumed to obey $U > c_n$. The solution of (11), and the corresponding equation for v^δ_n determined from (6*b*), are given below.

4.2. *Solution for a travelling front*

The solution for the *barotropic mode* ($n = 0, U < c_0$) is

$$u^\delta_0(\xi) = \frac{\bar{\tau}_0\,e^{-K|\xi|}}{2f(c_0^2/U^2-1)^{\frac{1}{2}}},\quad v^\delta_0(\xi) = -\frac{\bar{\tau}_0}{f}H(-\xi)-\operatorname{sgn}(\xi)\frac{\bar{\tau}_0}{2f}e^{-K|\xi|}, \tag{13}$$

where $H(x) = 0$ if $x < 0$ and 1 if $x \geqslant 0$, and

$$K \equiv \frac{f/c_0}{(1-U^2/c_0^2)^{\frac{1}{2}}}.$$

The solution for the *baroclinic modes* ($n \geqslant 1$, $U > c_1$) is

$$u_n^\delta(\xi) = -\frac{\bar{\tau}_n}{f}\frac{\sin k_n \xi}{(1-c_n^2/U^2)^{\frac{1}{2}}}H(-\xi), \quad v_n^\delta(\xi) = \left[-\frac{\bar{\tau}_n}{f}+\frac{\bar{\tau}_n}{f}\cos k_n \xi\right]H(-\xi). \tag{14}$$

For negative values of ξ the first term in v_n^δ, summed over all modes, gives

$$-\frac{1}{f}\sum_{n=0}^{\infty} \bar{\tau}_n \Psi_n = -\frac{\bar{\tau}}{fh}$$

in the surface layer, and zero below. This represents the Ekman drift in the surface mixed layer, which balances the wind stress at downstream distances a few times larger than $1/K \approx c_0/f$, the barotropic Rossby radius with a typical mid-latitude value of 2000 km. Closer to front the flow feels effects of the edge to the wind, so that the Ekman drift cannot be the only steady response. Here a sea-surface tilt results in a depth-independent geostrophic v, given by the decaying term in (13).

The total impulse response at a point (x, z) is determined by summing over the normal modes according to (4). It is argued below that the barotropic contribution to the u-field can be neglected. Using a fixed coordinate system, (14) gives

$$u^\delta(x,z,t) = -\sum_{n=1}^{\infty}\frac{\bar{\tau}_n}{f}\frac{\sin k_n(x-Ut)}{(1-c_n^2/U^2)^{\frac{1}{2}}}\Psi_n(z) = -\sum_{n=1}^{\infty}\frac{\bar{\tau}_n}{f^2}\omega_n \sin(k_n x - \omega_n t)\Psi_n(z), \tag{15}$$

where

$$\omega_n = Uk_n = \frac{f}{(1-c_n^2/U^2)^{\frac{1}{2}}} \tag{16}$$

are the allowed frequencies in the fixed frame.

4.3. *Solution for a travelling distributed wind*

Equation (15) represents the u-field due to a y-independent line source. For a wind-field distributed in x, assumed 'frozen' and propagating at uniform speed U, flow at a point $\mathbf{x} \equiv (x, z)$ is given by the superposition integral

$$u(\mathbf{x}, t) = \int_0^t [\tau_t^x(\alpha)+f\tau^y(\alpha)]\, u^\delta(\mathbf{x}, t-\alpha)\,\mathrm{d}\alpha. \tag{17}$$

For computing the impulse response u^δ used in (17), the stress jump $\bar{\tau}$ has to be set to unity.

4.4. *Discussion of the solution*

Although the solution (15) is surprisingly simple, it contains several features that agree with observations of inertial waves. Some properties of the solution are discussed below.

(i) The convergence of series (15) depends on several factors. For a depth-independent N and no mixed layer, the modal structure for horizontal velocity is $\Psi_n = \cos(n\pi z/D)$; equation (7) then gives $\bar{\tau}_n \approx 2\bar{\tau}/D = $ constant, implying that series (15) diverges. (The factor ω_n in the second form of (15) changes very little with n for common values of U, so that its effect on the convergence of series (15) can be neglected.) In the presence of a surface mixed layer the series does converge, but slowly. The convergence is faster if $N(z)$ decays sharply in the thermocline, which is sensible because only two modes are needed for a two-layer stratification. Calculations show that $\bar{\tau}_n$ may increase slightly for the lowest one or two baroclinic modes; for example, for $\overline{\tau} = 1$ dyn/cm^2 and the density profile shown in figure 6, $\overline{\tau}_0 = 40 \times 10^{-5}$, $\overline{\tau}_1 = 2.16 \times 10^{-5}$, $\overline{\tau}_2 = 2.18 \times 10^{-5}$, $\overline{\tau}_3 = 1.89 \times 10^{-5}$, $\overline{\tau}_4 = 1.62 \times 10^{-5}$ dyn/cm^3, and so on.

(ii) A comparison of (13) and (14) shows that the ratio of barotropic and baroclinic contributions to u^δ is of order

$$(U/c_0)\left(\tau_0 \Big/ \sum_{n=1}^{\infty} \overline{\tau}_n \Psi_n\right) \approx (U/c_0)(h/D)$$

which is negligible, while the same ratio for v^δ is of order

$$\left(\tau_0 \Big/ \sum_{n=1}^{\infty} \overline{\tau}_n \Psi_n\right) \approx h/D$$

which is small but non-negligible. However, the barotropic contribution here is non-oscillatory, and not of interest to us. Therefore, all numerical calculations will show the u-field only, and not the v-field which contains significant non-oscillatory parts.

(iii) The allowed frequencies ω_n are the points of intersection of the hydrostatic gravity wave dispersion relation $\omega^2 = f^2 + c_n^2 k^2$ with the straight line $\omega = Uk$ (figure 2). The relation $\omega = Uk$ picks out the phase speed ω/k at which the waves appear steady to an observer moving at speed U. Since c_n is the minimum phase speed of waves associated with mode n (see line $\omega = c_2 k$ in figure 2), U must exceed c_n for the straight line $\omega = Uk$ to intersect the dispersion relation. Note from figure 2 that c_n is also the maximum group speed. No transient wave for which $U < c_n$ can therefore be found ahead of the propagating wind.

(iv) Equations (13) and (16) show that the particle trajectory for each mode (or frequency) is elliptic, with an axis ratio of $u_n^{max}/v_n^{max} = (1 - c_n^2/U^2)^{-\frac{1}{2}} = \omega_n/f > 1$ and the major axis oriented along the direction of travel of the waves. This agrees with the well-known property that the axes ratio of rotational gravity waves of frequency ω equals ω/f (see for example Kundu 1990, p. 522).

(v) Equation (16) shows that all frequency components are larger than f, with $\omega_1 > \omega_2 > \omega_3, \ldots$, the higher modes converging toward the limit $\omega = f$. The second form of (15) shows that discrete spectral peaks are obtained at all ω_n, with the largest single spectral peak at ω_1 because both ω_1 and $\overline{\tau}_1$ are large. The inertial spectral peak due to the sum of all modes is blue shifted, because the higher modes (for which the various ω_n are close to f) contribute less to the sum. As observed, the amount of blue shift increases with depth, where lower modes dominate.

(vi) In the extreme case of very rapidly propagating wind ($U \gg c_1$), the frequencies of all modes are packed near f, with very little blue shift. The corresponding wavelength is $\lambda = 2\pi U/f$, which is large and referred to as the 'inertial wavelength'. In this case most of the inertial energy remains trapped in the surface mixed layer, with very little downward leakage into the thermocline.

(vii) In the opposite extreme, as U slows down and approahes c_1, the frequency components separate from the 'pack' one by one and move toward higher values, resulting in a large amount of downward leakage into the thermocline (see figures 3 and 4 of KT85).

(viii) Unless the waves survive dissipation for years, only a few low-order modes dominate the solution in the deep ocean, giving the impression of standing waves. This agrees with the observations of Fu (1981).

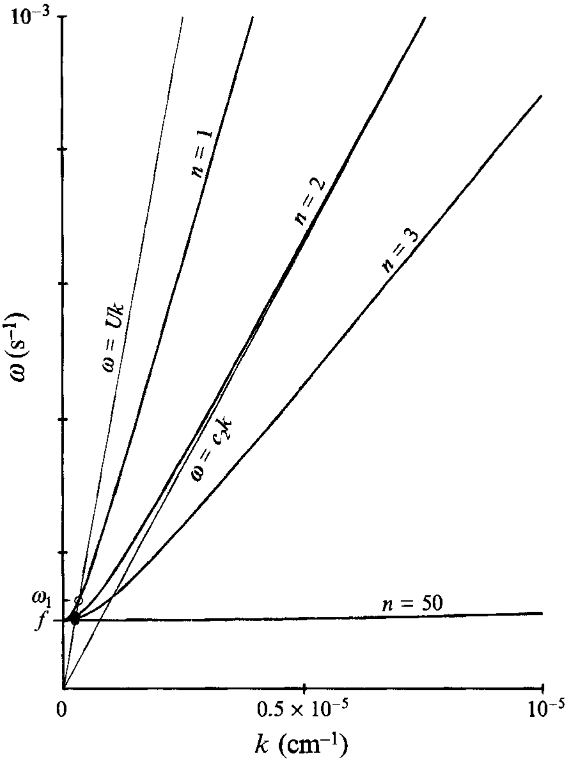

FIGURE 2. Plots of $\omega^2 = f^2 + c_n^2 k^2$ for $n = 1, 2, 3$, and 50, showing dispersion diagrams of hydrostatic internal wave modes. Line $\omega = c_2 k$ illustrates that c_2 is both the minimum phase speed and the maximum group speed of mode 2. Line $\omega = Uk$, with $U > c_1$, intersects all baroclinic dispersion relations at near-inertial frequencies $\omega_1, \omega_2, \ldots$. The values of parameters used are $U = 400$ cm/s, $f = 10^{-4}\ s^{-1}$, $c_1 = 253$, $c_2 = 132$, $c_3 = 88$ and $c_{50} = 5$ cm/s; these values of eigenspeed correspond to the density profile of figure 6.

4.5. *Consequences of non-hydrostatic dynamics*

Because the model makes the hydrostatic approximation in (2*e*), formula (16) is valid as long as ω_1 remains several times smaller than the local N. A solution to the equations of motion when the vertical acceleration w_t is included in (2*e*) is given by Fennel & Lass (1989) for a depth-independent N. However, consequences of the solution are not fully brought out there. Here we shall explore some of these consequences using simply the dispersion relation, without solving the differential equation.

For constant N the mode shapes of vertical velocity, which satisfy $w = 0$ at $z = 0, -D$, are of the form $\sin(m_n z)$, with the dispersion relation given by (Munk 1981)

$$\omega^2 = \frac{k^2N^2 + m_n^2 f^2}{m_n^2 + k^2}, \quad m_n D = n\pi, \quad n = 1, 2, \ldots. \tag{18}$$

The horizontal group velocity is then

$$G_n \equiv \partial\omega/\partial k = N^2 m_n^2 k (m_n^2 + k^2)^{-\frac{3}{2}} (k^2N^2 + f^2 m_n^2)^{-\frac{1}{2}}.$$

Setting $\partial G_n/\partial\omega = 0$, the maximum horizontal group speed is found to be

$$G_n^{max} = N/m_n = ND/n\pi = c_n \tag{19a}$$

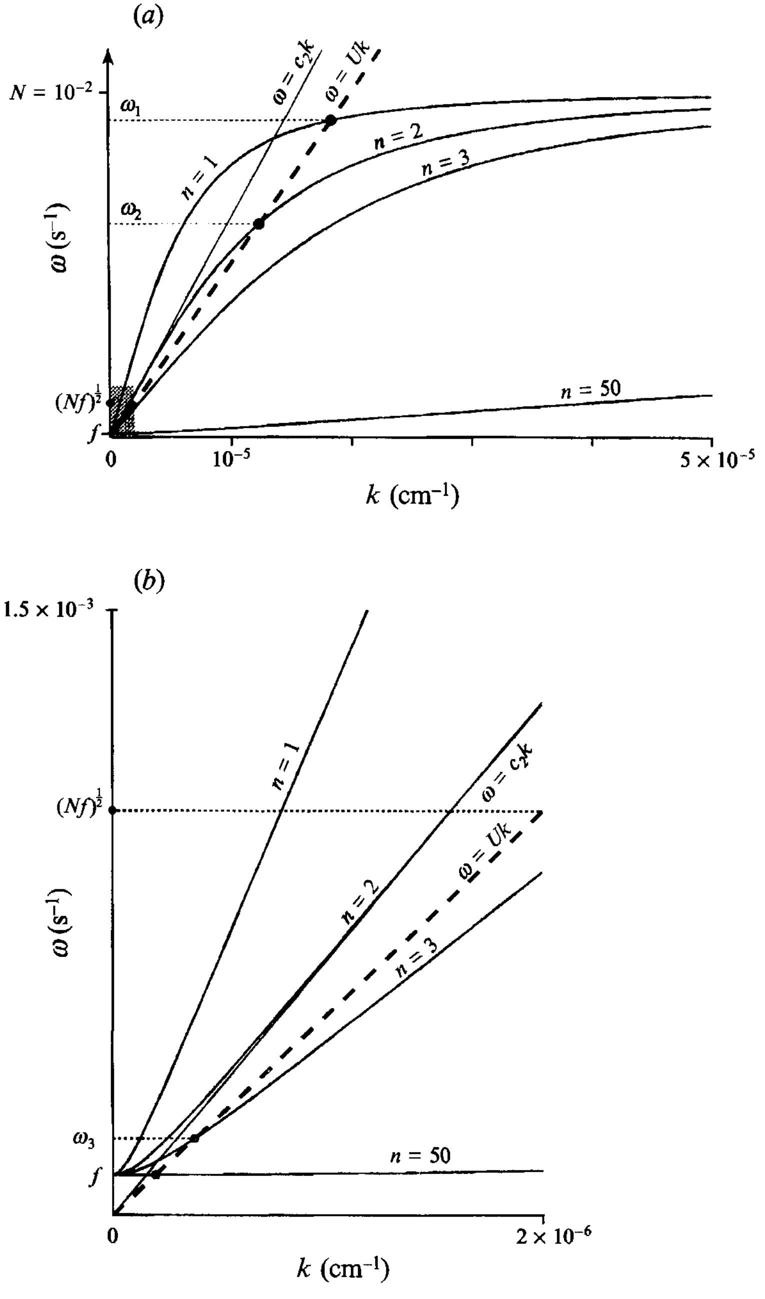

FIGURE 3. Plots of $\omega^2 = (k^2N^2+n^2\pi^2f^2/D^2)/(n^2\pi^2/D^2+k^2)$, with $c_n = ND/n\pi$, for $n = 1, 2, 3$, and 50, showing dispersion diagrams for non-hydrostatic internal wave modes in a constant-N ocean. In (*b*) an enlarged view of the shaded box in (*a*) is shown. Line $\omega = c_2 k$ is tangent to the dispersion diagram of mode 2 at the inflexion point where $\omega \approx (Nf)^{\frac{1}{2}}$, showing that c_2 is the maximum group velocity of mode 2. Line $\omega = Uk$, with $c_3 < U < c_2$, intersects the dispersion curves for $n = 1$ and 2 at frequencies above $(Nf)^{\frac{1}{2}}$; it also intersects the dispersion curves for $n = 3, 4, \ldots, \infty$ at frequencies below $(Nf)^{\frac{1}{2}}$. Values of parameters used are $N = 10^{-2}$ s^{-1}, $f = 10^{-4}$ s^{-1}, $D = 4$ km, and $U = 500$ cm/s.

which is reached at an inflexion point of the dispersion relation where the frequency–wavenumber pair is

$$\omega^{tran} \approx 3^{-\frac{1}{4}}(Nf)^{\frac{1}{2}} \approx (Nf)^{\frac{1}{2}}, \quad k \approx m_n(f/N)^{\frac{1}{2}} = \omega^{tran}/c_n. \tag{19b}$$

Taking $N = 10^{-2}\,\mathrm{s}^{-1}$ and $f = 10^{-4}\,\mathrm{s}^{-1}$, a typical period at the transition point is $2\pi(Nf)^{\frac{1}{2}} \sim 2$ hours. In deriving (19) it has been assumed that $N \gg f$, which is an excellent assumption in mid-latitude thermoclines where $N/f \sim 100$. The frequency ω^{trans} is independent of the mode number, and the superscript '*tran*' signifies 'transition' because the inflexion point seems to be a natural division between hydrostatic and non-hydrostatic waves. Note that $c_n = ND/n\pi$ also represents the maximum group speed of hydrostatic internal waves in a constant-N ocean. The reason it has the same significance in the transition region of a non-hydrostatic model, as (19*a*) shows, is that ω and k are not large enough at the inflexion point to be out of the hydrostatic range.

Figure 3 shows plots of the dispersion relation (18) for modes $n = 1$, 2, 3, and 50, assuming $f = 10^{-4}\,\mathrm{s}^{-1}$ and $N = 10^{-2}\,\mathrm{s}^{-1}$. Also included are plots of straight lines $\omega = c_2 k$ and $\omega = Uk$, where $c_3 < U < c_2$. It is seen that the line $\omega = c_2 k$ is tangent to the dispersion diagram for mode 2 at its inflexion point, so that the maximum horizontal group speed of a mode is indeed c_n, consistent with (19*a*). Moreover, a line $\omega = c_n k$ remains almost tangent to the dispersion diagram of mode n for a large range of ω, so that only for about $\omega > 5(Nf)^{\frac{1}{2}}$ do the waves start to become non-hydrostatic. The minimum phase speed tends to be vanishingly small as $k \rightarrow \infty$. In the hydrostatic case, on the other hand, figure 2 shows that the eigenspeed c_n has the dual significance of being the maximum group speed as well as the minimum phase speed.

An interesting consequence of removing the hydrostatic assumption is the generation of internal waves of all modes in the wake of a propagating wind, whatever the value of U. The excited frequencies fall into two ranges, a low-frequency range $f < \omega < (Nf)^{\frac{1}{2}}$ for rapidly travelling winds ($U > c_n$), and a high frequency range $(Nf)^{\frac{1}{2}} < \omega < N$ for slowly travelling winds ($U < c_n$). As an example, consider the line $\omega = Uk$ in figure 3, for which $c_3 < U < c_2$. It intersects modes $n = 1$ and 2 at frequencies above $(Nf)^{\frac{1}{2}}$ (see figure 3*a*), and all higher modes at frequencies below $(Nf)^{\frac{1}{3}}$ (see figure 3*b*). Generalizing, for a propagation speed in the range $c_{n+1} < U < c_n$, the lower modes $(1, \ldots, n)$ generate high-frequency waves and all the higher modes generate low-frequency waves. The frequency interval $f < \omega < (Nf)^{\frac{1}{2}}$ could be regarded as the 'hydrostatic range', while $\omega \gg (Nf)^{\frac{1}{2}}$ could be called the 'buoyancy range'.

A frequently observed feature in the spectra of vertical displacement of isotherms in the thermocline is a broad peak (or shoulder), and high vertical coherence, somewhat below the local buoyancy frequency (figure 4). This feature has been explained (Desaubies 1975; Munk 1980) as a local phase coupling (that is, constructive interference) between the incident and reflected waves near the local turning depth in the thermocline at which $\omega = N$. However, the constant-N numerical calculations of Shen & Holloway (1986), in which there are no turning depths, showed a spectral peak near N due to nonlinear wave interactions. They also raise the point that the observations of Levine *et al.* (1983*a*) and Levine, de Szoeka & Niiler (1983*b*), made close to the surface layer where the N-profile is not expected to support significant wave turning, showed a spectral peak and high vertical coherence near N.

The discussion of this subsection provides the following alternative and promising explanation for this spectral feature. Figure 3(*a*) shows that for a large range of slow propagation speeds the $\omega = Uk$ line can intersect the dispersion diagrams of a few low-order baroclinic modes at values of ω somewhat below N. Moreover, the horizontal group speed at these points is small, so that the wave energy will not escape quickly to

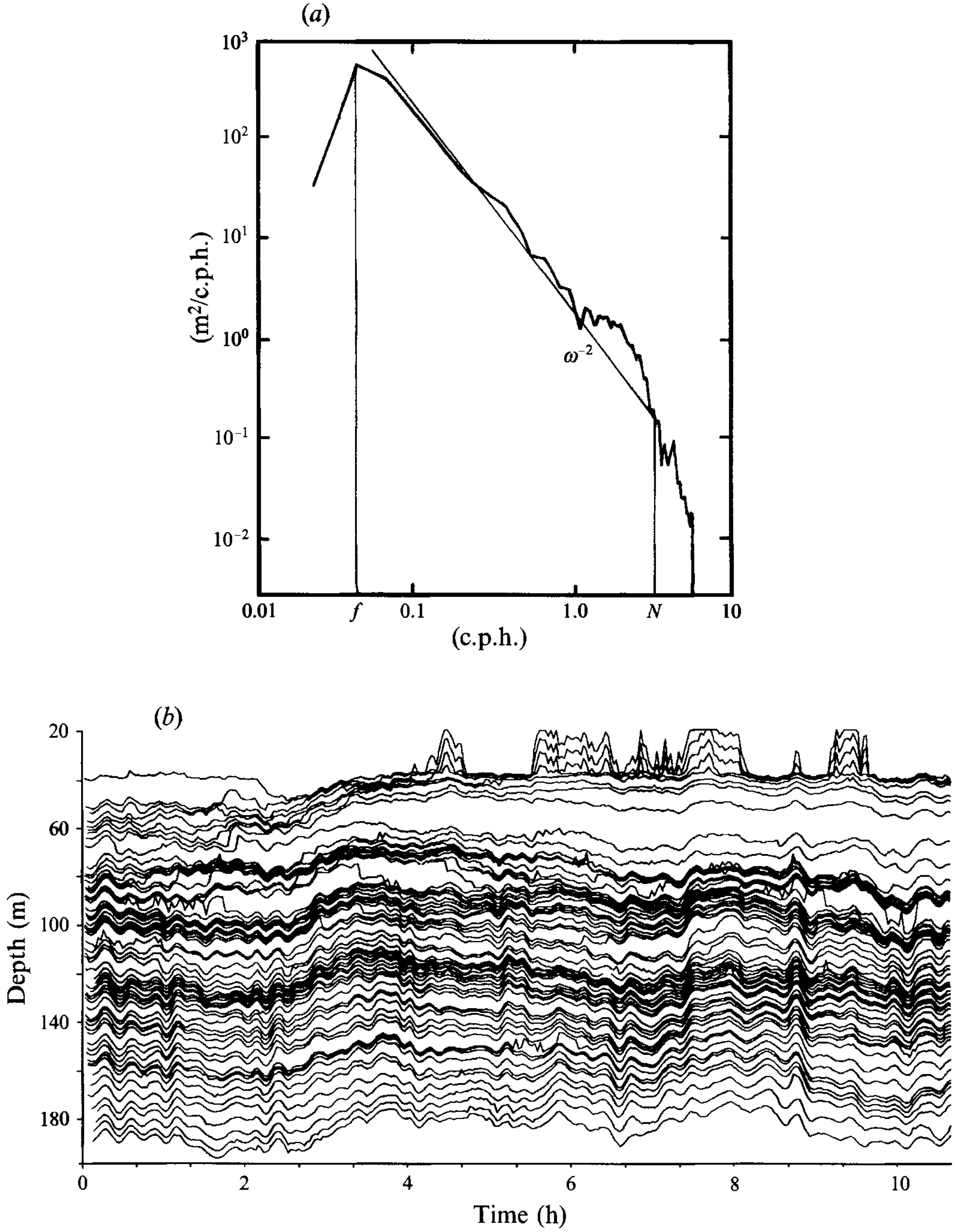

FIGURE 4. (*a*) Observed spectrum of vertical displacement of 6.6 °C isotherm, measured at a depth of about 350 m in a location 800 km off San Diego. Note the increase of energy level just below the local buoyancy frequency *N*, followed by an abrupt cutoff. (From Cairns & Williams 1976.) (*b*) Depth–time plot of the vertical displacement of isotherms in the thermocline, observed off the coast of California. Sixty-four isotherms separated by about 0.1 °C are followed over a 10 hour period. Note that the high-frequency waves occur in groups of one to three, and exhibit remarkable phase coherence with depth; lower-frequency motions have greater displacements and show greater phase variability. (From Pinkel 1981.)

a location where the frequency may not bear such a relationship to the local N. These features essentially agree with the observations of Pinkel (1975, 1981, 1985) and Levine *et al.* (1983*a*, *b*), who noticed that at high frequencies the vertical motion has a simple vertical structure, and is strongly correlated vertically, the first mode becoming increasingly prominent at higher frequencies.

The argument given here is qualitative because N has been assumed constant, while the resulting dispersion relation has been used to explain a phenomenon in the thermocline. For a depth-dependent $N(z)$, the vertical modes of non-hydrostatic internal waves depend on ω. For $\omega < N_{max}$, the modes are oscillatory between the turning depths (where $\omega = N(z)$), outside of which they decay exponentially; see for example figure 5.10 of Phillips (1977), or figure 5 of Garrett & Munk (1979). The first baroclinic mode represents an up–down, in-phase motion of the vertical column between the turning depths in the thermocline, not of the entire ocean. The vertical displacement for mode 1 is maximum in the middle of the thermocline, and figure 4(*b*) does suggest such a behaviour.

The validity of the explanation given here relies on the fact that the local dispersion relation should resemble the one given in figure 3 even when the density structure has a thermocline, simply because ω is bounded from above by the local N (see figure 3 of Garrett & Munk 1972). The arguments given here to explain the peak and coherence of vertical motion are therefore valid, although the range of values of U which produces the best simulation of the observations will be different. Further discussion of this point is provided in the concluding section.

5. Solution for variable f

As discussed above, inertial waves are greatly influenced by the variation of the Coriolis parameter with latitude. In order to determine how the constant-f solutions discussed in the previous section are affected by the variation of f with latitude, the hydrostatic set (6) is solved with $f = 2\Omega \sin\theta$. Consider a y-independent wind field $[\tau^x, \tau^y]$ moving eastward at speed U. Because of the variation of f with y, however, the problem is not y-independent, and requires a numerical solution. The latitude range of the region of integration is taken to be 20° N to 40° N (figure 5). The flow induced by a line front moving eastward is examined in §§5.2–5.4. The general case of an observed wind series, assumed 'frozen' and propagating eastward, is considered in §5.5.

5.1. *Method of calculation*

Making the moving coordinate substitution $\partial_t \rightarrow -U\partial_\xi$, equations (6) become

$$u_{n\xi} = -\frac{U}{U^2-c_n^2}\left[\tau_n^x + fv_n + \frac{c_n^2 v_{ny}}{U}\right], \quad p_{n\xi} = \frac{c_n^2}{U}[u_{n\xi}+v_{ny}], \quad v_{n\xi} = -\frac{1}{U}[\tau_n^y - fu_n - p_{ny}]. \tag{20a–c}$$

The set (20) is integrated downstream as an initial value problem with starting conditions $u_n = v_n = p_n = 0$ for $\xi \leqslant 0$.

The conditions at the northern and southern boundaries posed a problem. A radiation condition allowing the energy to leave at these boundaries would be proper if the forcing were confined within the region, as in the moving cyclone problems of Price (1983) and Greatbatch (1983). This technique, however, does not work in the present problem which simulates the response to a travelling y-independent wind, for which some of the blue-shifted waves will travel slightly poleward, entering the region

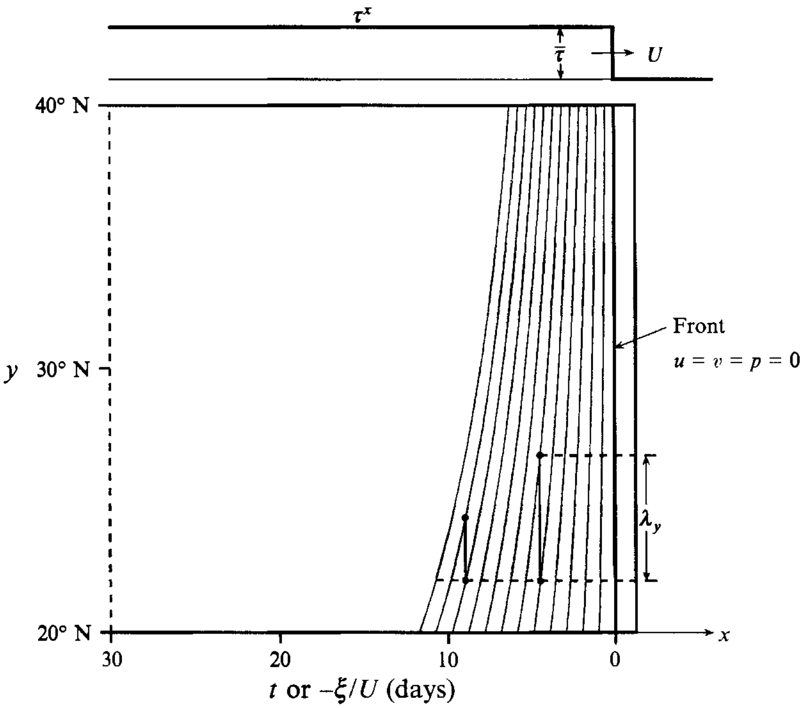

FIGURE 5. Region of integration. The moving front is shown at the top of the figure. Several constant-phase lines are sketched in to illustrate the decrease of λ_y with time. Wave frequencies decrease at lower latitudes due to the decrease of $f(y)$, resulting in bending of the constant-phase lines.

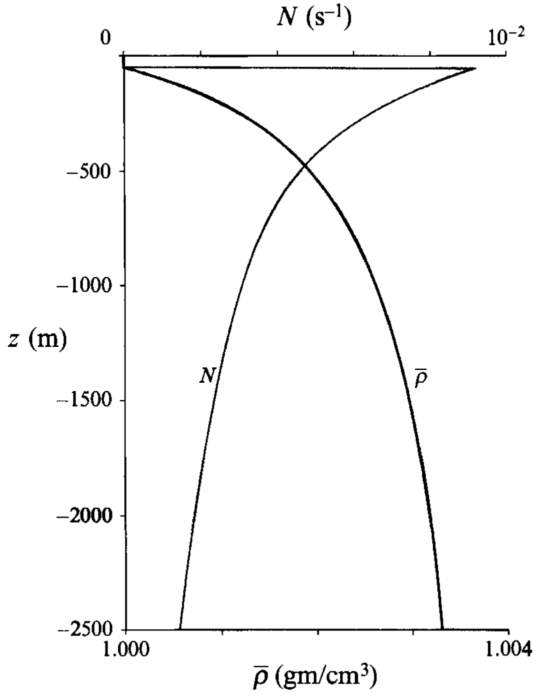

FIGURE 6. Vertical distributions of background density given by (21 *c*, *d*), and the resulting buoyancy frequency used in the model calculations.

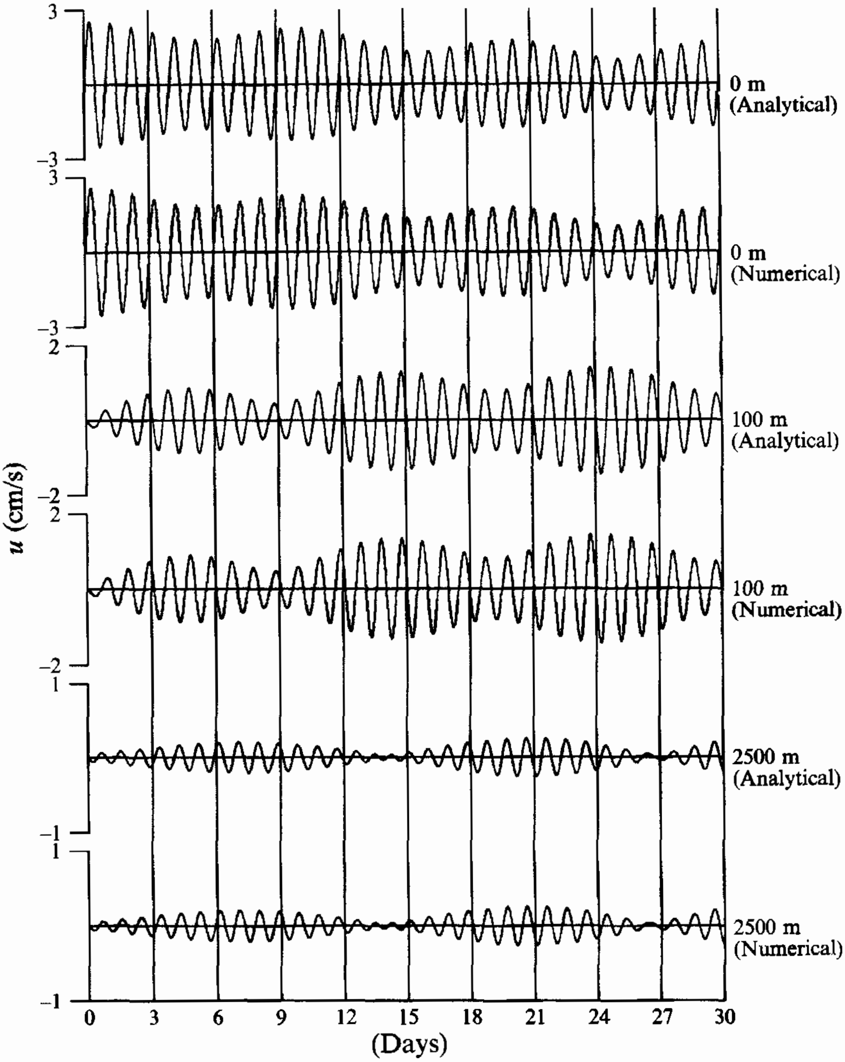

FIGURE 7. Comparison of analytical and numerical solutions at depths of 0, 100, and 2500 m. Parameters used are $U = 600$ cm/s, and a constant value of $f(30° \text{ N}) = 0.7247 \times 10^{-4} \text{ s}^{-1}$. Note the excellent agreement of the numerical and analytical solutions, and the intermittency of the wave amplitude.

of integration through the southern boundary. The propagation along characteristics will not work near the southern boundary for the same reason, since one cannot follow the solution along the poleward-going characteristic near this boundary. Several schemes given in Orlanski (1976) were tried, but each of them produced some distortion near the southern boundary. We finally decided to use the simple condition of zero normal derivative at the northern and southern boundaries, which did not produce any more distortion than the Orlanski schemes. The distortion near the northern boundary caused by this condition was negligible, as can be expected from the schematic phase lines in figure 5. In fact, the distortions were essentially confined to the region south of 35° N, and (except figure 11) all results displayed here are north of this latitude.

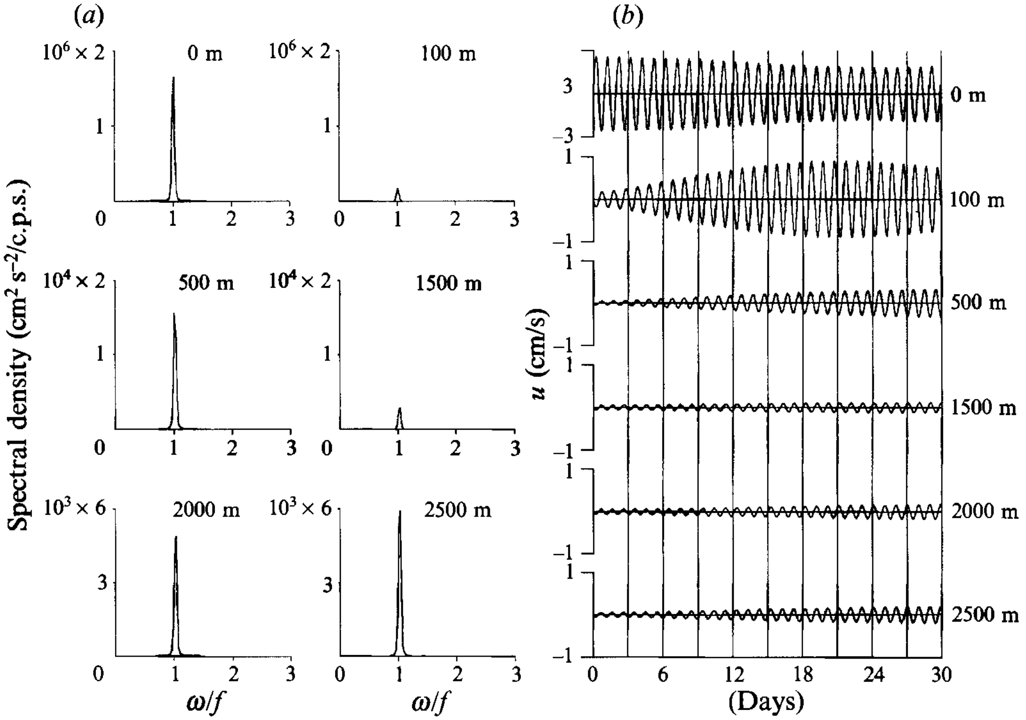

FIGURE 8. Flow due to a fast front moving eastward at $U = 1200$ cm/s, using a constant value of $f(30° \text{ N}) = 0.7247 \times 10^{-4}$ s^{-1}. (*a*) High-resolution spectra of $\overline{u^2}$, with two degrees of freedom and a bandwidth of $0.018f$. Vertical scales are exaggerated at larger depths. Note the dominance of $\omega_1 = 1.023f$ below the zero crossing of mode 1 at 960 m. (*b*) Time series of u, showing the low intermittency.

Although real storms last only about a week, the integration is carried up to $|\xi|_{max}/U = t_{max} = 30$ days in order to understand the development of the solution for large times. The downstream grid size is taken as $\Delta\xi/U = \Delta t = 30$ min. Since the system is hyperbolic, numerical stability requires that the grid slope $\Delta y/\Delta\xi$ be greater than the characteristic slope $\mathrm{d}y/\mathrm{d}\xi \approx (U^2/c_n^2 - 1)^{\frac{1}{2}}$, which is maximum for the first mode. Choosing a factor of 1.1, the latitudinal grid size is set at $\Delta y = 1.1\Delta\xi(U^2/c_1^2 - 1)^{-\frac{1}{2}}$. For a typical propagation speed of $U = 600$ cm/s, these criteria imply $|\xi|_{max} = 15550$ km, $y(40° \text{ N}) - y(20° \text{ N}) = 2222$ km, $\Delta\xi = 10.8$ km, and $y = 5.5$ km. The magnitude of ξ_{max} is larger than the zonal width of any ocean, which is why the integration is stopped after 30 days. After the finite-difference solution of the modal coefficients in (20), the complete solution is obtained by summing over 100 vertical modes, as indicated in (4).

The mode shapes $\Psi_n(z)$ and the values of c_n are determined by solving the eigenvalue problem (5). The oceanographic parameters used are

$$D = 2500 \text{ m}, \quad h = 50 \text{ m}, \qquad (21a, b)$$

$$\bar{\rho} = \begin{cases} 1 \text{ gm/cm}^3 & \text{for } z \geqslant -h, \qquad (21c) \\ 1 + \Delta\rho_1[1 - \mathrm{e}^{(z+h)/b_1}] + \Delta\rho_2[1 - \mathrm{e}^{(z+h)/b_2}] \text{ gm/cm}^3 & \text{for } z < -h, \qquad (21d) \end{cases}$$

where $\Delta\rho_1 = 0.00125$ gm/cm^3, $b_1 = 200$ m, $\Delta\rho_2 = 0.00225$ gm/cm^3, and $b_2 = 1000$ m. The assumed background density profile $\bar{\rho}(z)$ implies a surface mixed layer of thickness (*a*) $\theta = 25°$ N

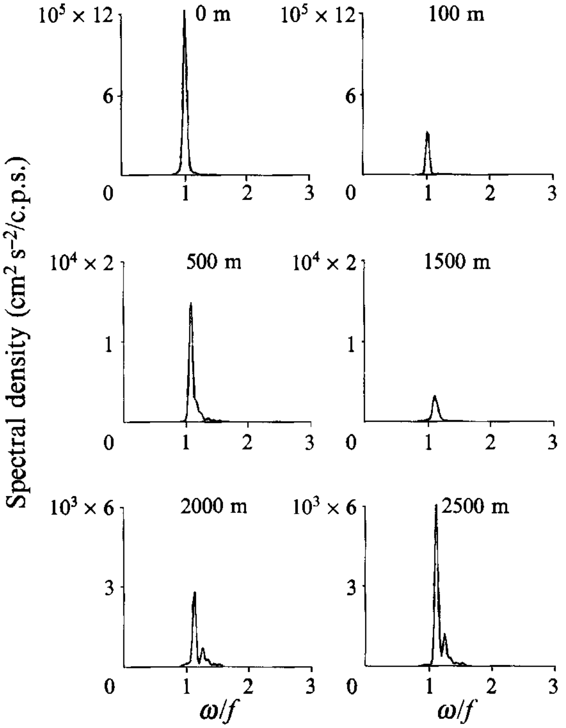

(*b*) $\theta = 35°$ N

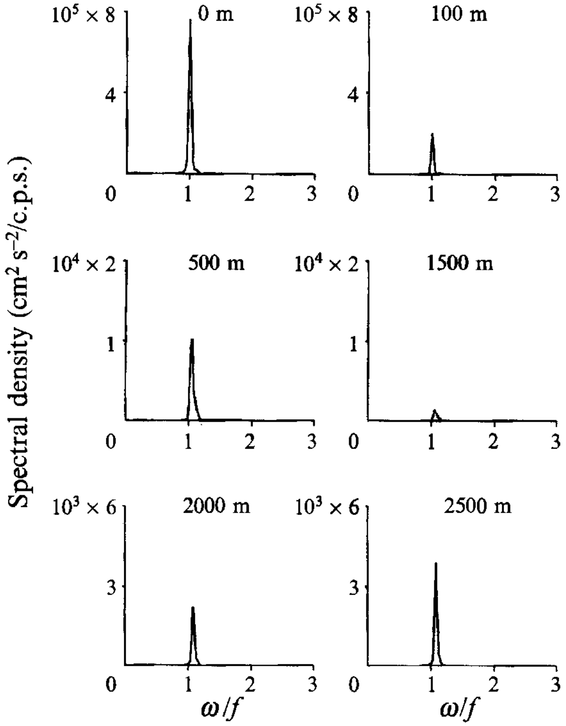

FIGURE 9. Flow due to a fast front moving eastward at $U = 1200$ cm/s using a variable-f model, showing spectra of $\overline{u^2}$ at (*a*) 25° N and (*b*) 35° N at various depths. Note that the spectra at 25° N contain a wider range of frequencies than the spectra at 35° N, because the waves arriving here have been generated in a wider range of latitudes in the north.

$h = 50$ m, and a thermocline just below the mixed layer where $N_{max} = 0.89 \times 10^{-2}\ \mathrm{s}^{-1}$ (figure 6). The eigenvalue problem is solved by taking 5000 points in the vertical, resulting in a fine vertical resolution of $\Delta z = 0.5$ m. The so-called 'shooting method' is used, which involves assumption of a value for c_n, integration of (5) from the sea surface with the boundary conditions $\Psi_n(0) = 1$ and $\Psi_{nz}(0) = 0$, and checking to see if the condition $\Psi_{nz}(-D) = 0$ is satisfied at the ocean bottom. If not, the procedure is repeated with a different value of c_n, until the boundary condition at the ocean bottom is satisfied. The iteration procedure is automated so that the various possible solutions are found in order of increasing n, starting with $n = 1$. Altogether, 100 modes are determined. The first three baroclinic eigenspeeds are found to be $c_1 = 252.6$, $c_2 = 132.0$, and $c_3 = 87.9$ cm/s. The barotropic mode does not satisfy the rigid-lid condition used here; for $n = 0$ we use the known solution $\Psi_0(z) = 1$ and $c_0 = (gD)^{\frac{1}{2}} = 20000$ cm/s. After finding the eigenfunctions on 5000 vertical points, their values are saved on only 100 vertical points, at intervals of 25 m; they define the depths at which the flow field is evaluated.

The accuracy of the finite-difference calculations is checked by comparing the u-field computed from (20) with that computed from analytical solution (15). Parameters chosen for this comparison are a sharp front with a jump in τ^x of $\bar{\tau} = 1$ dyn/cm^2, a constant value of $f(30° \mathrm{N}) = 0.7247 \times 10^{-4}\ \mathrm{s}^{-1}$, and $U = 600$ cm/s. Figure 7 shows the resulting time series of $u(t) = u(-\xi/U)$ at depths of 0, 100 and 2500 m. (The independent variable in these series can be regarded either as time in fixed frame, or as (downstream distance)/U in moving frame.) Except for a slight phase lead of the numerical solution at all depths, the series are practically indistinguishable.

Results will now be presented for the u-field generated by three values of the frontal propagation speed: $U = 1200$ ('fast'), 600 ('medium'), and 300 cm/s ('slow'), using a variable f.

5.2. *Results for fast front* ($U = 1200$ *cm/s*)

Consider a front propagating at $U = 1200$ cm/s. As a prelude, figure 8 shows the time series and variance spectra of u at several depths for a constant value of $f(30° \mathrm{N}) = 0.7247 \times 10^{-4}\ \mathrm{s}^{-1}$. At this high value of U, equation (16) shows that all values of ω_n are close to f, with $\omega_1 = 2.3\%$ above f, $\omega_2 = 1.2\%$ above f, and so on. Consequently, the spectral peaks (figure 8*a*) are very thin, and the separate components $\omega_1, \omega_2, \ldots$, are not resolved even with the smallest possible bandwidth $1/t_{max}$ used in the spectral calculation. The intermittency, being the result of interference of waves of different frequencies, is small (figure 8*b*). The spectral peak in the surface layer is practically centred on f, while the peaks in the deep ocean (1000–2500 m) are slightly blue shifted, implying the dominance of low-order modes in the deep ocean. As explained by Gill (1984) in the context of a different problem, all modes are in phase at $t = 0$, their sum amounting to a flow confined in the surface mixed layer and rotating clockwise at an angular speed $\omega \approx f$. However, mode 1 rotates at a larger angular speed ω_1, and reveals its maximum amplitude below the mixed layer when it develops a 90° phase difference in time $t_1 = \frac{1}{2}\pi/(\omega_1 - f) = 10.9$ days. Similarly, mode 2 does the same in time $t_2 = 20.8$ days. The 'beating time' (one lobe of the amplitude envelope) in the deep ocean is due mainly to the interference of modes 1 and 2, and has the magnitude $2\pi/(\omega_1 - \omega_2) = 77$ days. This is consistent with figure 8(*b*), where a little less than half the lobe shows up in 30 days. Although mode 1 takes 10.9 days to develop its maximum amplitude in the deep ocean, it starts to appear immediately. This energy does come from the surface layer, but zonal sections do not show a gradual leakage of energy from the surface layer. This is because the concept of wave groups becomes meaningful only when a number of modes are superposed.

Now consider the results of the variable-f model. Figure 9 shows the spectra of $\overline{u^2}$ along 25° N and 35° N at various depths. The spectra at 35° N are not too different than those in the constant-f model (figure 8a), except that the peaks are slightly more blue shifted and wider. The reason for this is the southward propagation of the inertial waves, to be discussed shortly. The spectra at 25° N in the variable-f model show more structure. They contain a wide range of frequencies, and a close examination shows that the high-frequency waves at this latitude are generated at higher latitudes, and have travelled southward. For example the ω_1 generated locally at 40 °N is the highest frequency found at 25 °N. Use of (16) shows that

$$\omega_1 \text{ at } 40° \text{ N} = 1.56f(\text{at } 25° \text{ N}) \rightarrow \omega_{max}/f = 1.56 \text{ at } 25° \text{ N}. \quad (22)$$

That is, the highest frequency found at 25° N is about 1.56 times the local value of f, in good agreement with the near-bottom spectra in figure 9. Owing to the wider range of frequency content, the time series of u at 25° N are considerably more intermittent than those at 35° N (figure 10).

The southward propagation of wave energy is illustrated in figure 11, which shows yz-sections of the u-field at $t = 8.31$ and 24.98 days. In agreement with (1), the field indeed develops a north–south wavelength of $\lambda_y = 2\pi/\beta t$ due to the latitudinal variation of f. Taking $\beta = 2\Omega \cos 30°/R_e = 1.708 \times 10^{-3}$ day^{-1} km^{-1}, we get

$$\lambda_y \approx 442 \text{ km at } t = 8.31 \text{ days}, \quad \text{and} \quad \lambda_y = 147 \text{ km at } t = 24.98 \text{ days}.$$

These estimates agree fairly well with figure 11, where every other zero contour is separated by one wavelength. A closer examination reveals that the value of λ_y increases slowly with latitude; this again is in agreement with $\lambda_y = 2\pi/\beta t$, and the fact that β decreases with latitude. (On the horizontal plane, the decrease of λ_y with time is schematically shown in figure 5.)

Compared to the constant-f model, the vertical correlation of u was found to be smaller in the variable-f model. This is discussed in greater detail for a slower propagation speed of $U = 600$ cm/s.

5.3. *Results for medium-speed front* ($U = 600$ *cm/s*)

The main effects of decreasing the speed of propagation are to decrease λ_x, increase the frequency bandwidth, and hasten the leakage of energy from the surface layer. As a prelude, it is useful to examine the constant-f solution first (figure 7). Formula (16) gives $\omega_1 = 10.3\,\%$ above f, $\omega_2 = 2.5\,\%$ above f, and so on. The intermittency below the mixed layer is caused by the interference of waves that have penetrated to these depths. At 100 m, a spectral calculation shows a primary peak slightly above f resulting from the penetration of several higher modes, and a secondary peak at ω_1, giving an approximate 'beating' period of $2\pi/(\omega_1 - f) = 9.74$ days. At 2500 m, on the other hand, only the first two modes with their relatively high frequencies ω_1 and ω_2 have made their presence felt in 30 days, giving a beating period of $2\pi/(\omega_1 - \omega_2) = 12.87$ days. These values of the beating period are in very good agreement with figure 7.

Now consider the results of the variable-f model. Figure 12 shows the spectra of $\overline{u^2}$ along 25° N and 35° N at various depths. Compared to the fast front (figure 9), the energy is now spread over a wider range of frequency, as expected from the larger values of ω_1 and ω_2. The comparison of the two spectra also shows that figure 12 has less energy in the surface layer and more energy below. This is due to a faster leakage from the surface layer due to greater horizontal inhomogeneity (shorter λ_x). Owing to the southward propagation of energy, a relation such as (22) holds again, with the

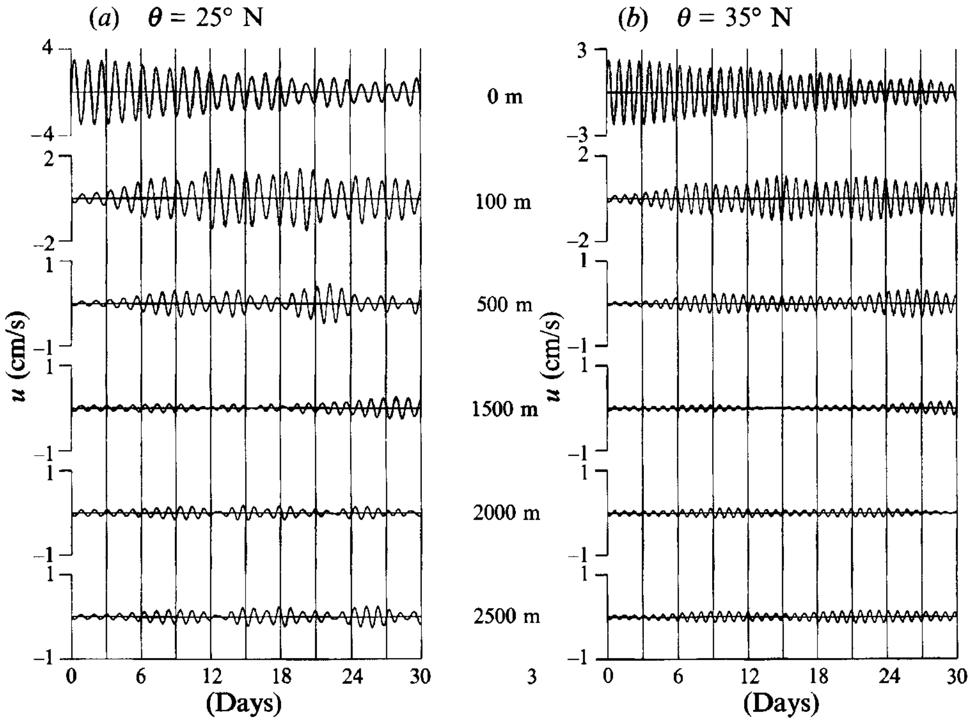

FIGURE 10. Flow due to a fast front moving eastward at $U = 1200$ cm/s using a variable-f model, showing time series of u at (*a*) 25° N and (*b*) 35° N at various depths. Note that the series at 25° N are far more intermittent than the series at 35° N.

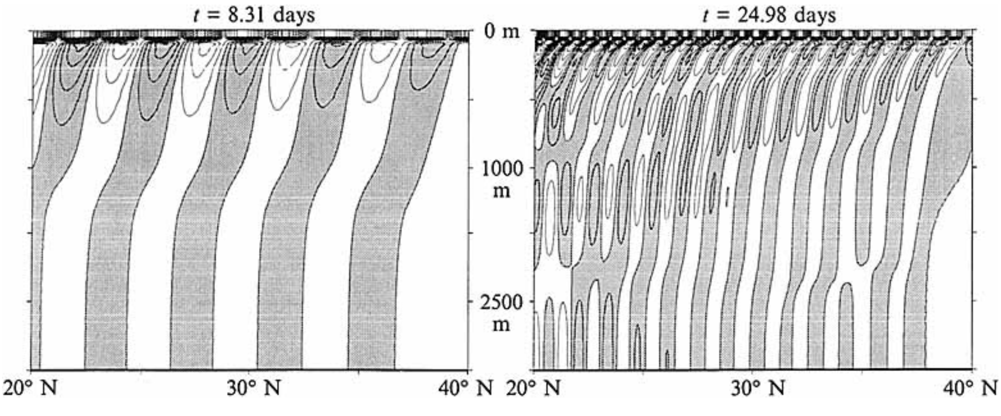

FIGURE 11. Flow due to a fast front moving eastward at $U = 1200$ cm/s using a variable-f model, showing y, z-sections of the u-field at $t = 8.32$ and 24.98 days. Negative regions are shaded. Note the decrease of λ_y with time, the slow increase of λ_y with latitude, and the increased energy in the south at larger time, implying equatorial propagation of the waves.

factor on the right-hand side now being 1.68. At 35° N, a secondary peak close to ω_1 now clearly stands apart from the primary peak, especially at depths greater than 2000 m. The intermittency of the two deepest time series at 35° N is therefore larger (figure 13) than for the faster propagation speed (figure 10). At 25° N the spectral (*a*) $\theta = 25°$ N

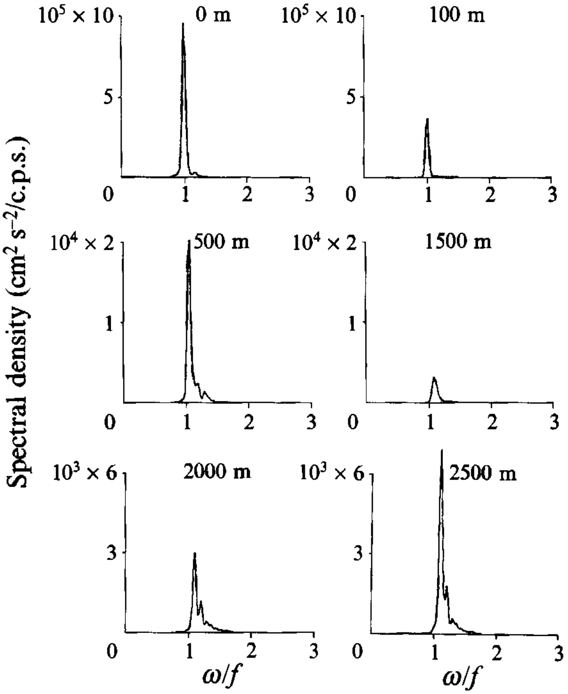

(*b*) $\theta = 35°$ N

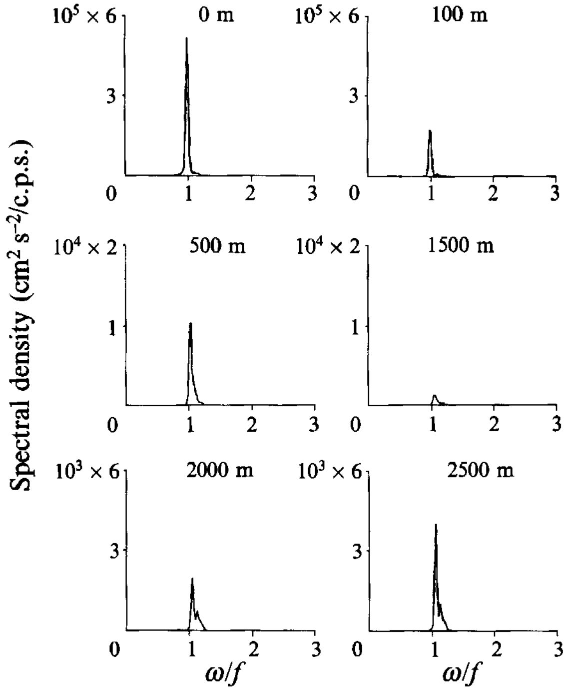

FIGURE 12. Flow due to a medium-speed front moving eastward at $U = 600$ cm/s using a variable-f model, showing spectra of $\overline{u^2}$ at 25° N and 35° N at various depths. Vertical scales are exaggerated at larger depths. Note that the spectra at 25° N contain a wider range of frequencies than the spectra in 35° N, because the waves arriving here have been generated in a wider range of latitudes in the north.

widths are larger, and the first secondary peak is somewhat above the local ω_1, presumably due to the equatorward propagation of waves from higher latitudes.

The correlation of u for three values of the vertical separation is shown in figure 14. A large number of modes contribute in the thermocline (left column). The range of contributing modes is larger in the variable-f model because the horizontal inhomogeneity arising out of the variation of f causes a faster leakage from the surface layer. The waves generated by the various modes are not in phase at a point, because they originate at different latitudes. This reduces the vertical correlation compared to the constant-f model. In the deep ocean (right column), on the other hand, vertical correlation is high in spite of the large spectral width, because only one or two modes dominate. This agrees with the observations quoted in §2, namely that the vertical structure in the deep ocean frequently appears as standing waves.

5.4. *Results for slow front* ($U = 300$ *cm/s*)

The same basic effects of a smaller λ_x, a larger frequency bandwidth, and a faster leakage of energy from the surface layer continue as the speed of propagation is decreased to $U = 300$ cm/s. The allowed frequencies in the constant-f model are $\omega_1 = 83.4\%$ above f, $\omega_2 = 11.4\%$, above f, and so on. The hydrostatic assumption still holds, since $[\omega/\omega^{tran}]_{max} = [1.83f/3^{-\frac{1}{4}}(fN)^{\frac{1}{2}}]_{max} = [2.41(f/N)^{\frac{1}{2}}]_{max} = 0.70 < 1$; the largest value is achieved on the ocean bottom at 40° N. Only the spectra are shown for this case (figure 15). A relation such as (22) gives the factor on the right-hand side to be 2.82; however, little energy is evident at this frequency in the deep spectra at 25° N. This is because the local value of $\omega_1/f = 1.834$ is quite high in this case, resulting in a fast downward leakage and domination of the deep flow by the modes excited locally by the travelling wind effect. Moreover, for variable f the maximum local frequency is not ω_1, but increases with t because $k_y = \beta t$ increases with t. Assuming that the high-frequency waves should be present in the solution for about 4 days in order that they are able to show up in the spectra, an appropriate 'maximum' value for zonal wavenumber is $k_y = \beta t = \beta \times (26 \text{ day}) = 4.4 \times 10^{-7}$ cm^{-1}. The travelling effect introduces a zonal wavenumber whose maximum value (using (12) and mode 1) is $k_x = 2.77 \times 10^{-7}$ cm^{-1}. With these values, the dispersion relation $\omega_1^2 = f^2 + c_1^2(k_x^2 + k_y^2)$ gives $\omega_1/f(25° \text{ N}) = 2.36$, in fair agreement with figure 15. (Such an argument does not work for $U = 1200$ and 600 cm/s, when the local downward leakage does not dominate the propagation from higher latitudes.) The vertical correlation (not shown) is now lower than in the case of $U = 600$ cm/s, because the increased horizontal inhomogeneity has caused a large number of modes to contribute to the flow.

5.5. *Results for observed wind*

A calculation is now presented using a time series of wind stress observed at a fixed point near the coast of British Columbia (top plots of figure 16*b*, *c*). During the period of observation, inertial waves were generated by warm and cold fronts propagating at speeds in the range $U \sim 420$–830 cm/s, features of which are reported by Thomson & Huggett (1981) and KT85. Four large fronts propagated nearly eastward during the second week of the wind-stress series shown in the figure, and generated inertial waves of maximum amplitude 75 cm/s in the surface layer, and 5–7 cm/s at a depth of 160 m near the shelf bottom. The object here is not to simulate the frontal response in shallow water, but to illustrate the superposition of responses due to various wind events during a month. This can be achieved by calculating the responses to the wind-stress series shown in figure 16, the entire series assumed to be 'frozen' and propagating eastward at $U = 600$ cm/s.

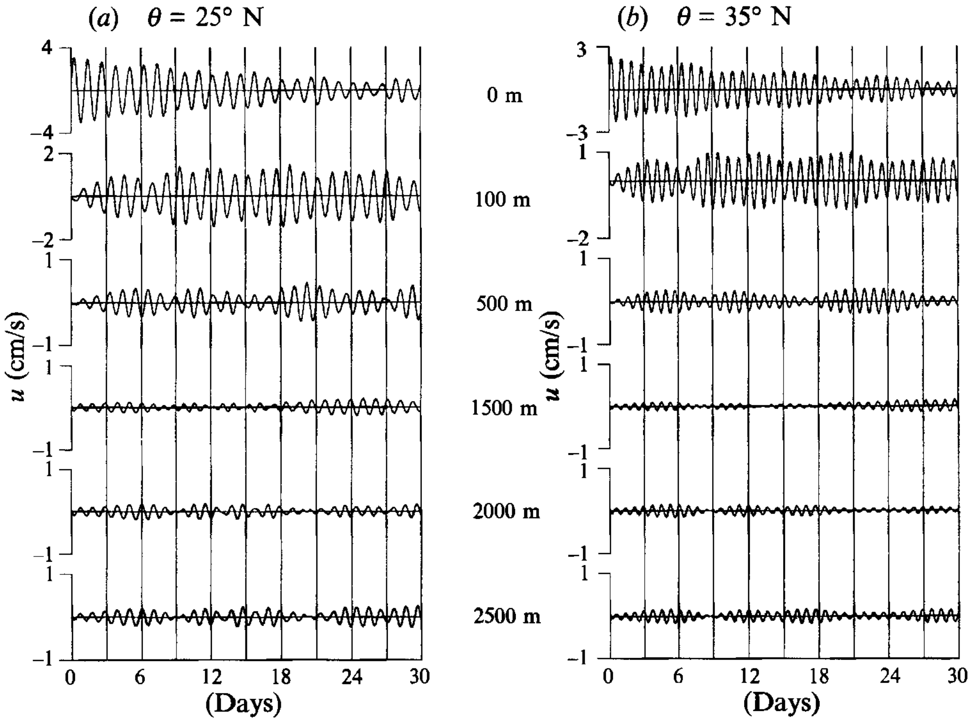

FIGURE 13. Flow due to a medium-speed front moving eastward at $U = 600$ cm/s using a variable-f model, showing time series of u at 25° N and 35° N at various depths. Note that the series are 25° N are far more intermittent than the series at 35° N.

The spectra in figure 16 are qualitatively similar to those for the response to a front, except that they are coloured by the spectra of the wind forcing. Let $\phi(t) \equiv \tau_t^x(t) + f\tau^y(t)$ be a stationary wind forcing, and $(\hat{\ })$ denote Fourier transform. Then a transform of (17) gives

$$\hat{u}(\omega) = \hat{\phi}(\omega)\,\hat{u}^{\delta}(\omega) \rightarrow S_u(\omega) = |\hat{u}^{\delta}(\omega)|^2\, S_{\phi}(\omega), \tag{23}$$

where S_u is the spectrum of $u(t)$, $S_{\phi} = \omega^2 S_{\tau^x} + f^2 S_{\tau^y}$ is the spectrum of $\phi(t) \equiv \tau_t^x(t) + f\tau^y(t)$, and $\hat{u}^{\delta}$ is the frontal response or 'transfer function'. Equation (23) shows that the response at a particular ω is proportional to the strength of the wind forcing at that ω, modulated by the magnitude of the transfer function. There is no response at a particular ω if the forcing does not have energy at the same ω, which is a characteristic of all linear forced systems. A calculation showed that S_{ϕ} increases with ω for the wind series shown in figure 16, which is not unexpected since the first term for S_{ϕ} is proportional to ω^2. This is why there is more high-frequency content in figure 16(*a*) than in the response due to a front propagating at the same U (figure 12), for which $\phi(t) = \tau\delta(t)$ and S_{ϕ} is white. Time series plots of figure 16 show amplitudes of order 4 cm/s for depths larger than 2000 m, and that they are in the form of standing waves.

6. Summary and comments

Generation of internal waves in an ocean due to the zonal propagation of a y-independent wind field has been investigated by extending the hydrostatic constant-f

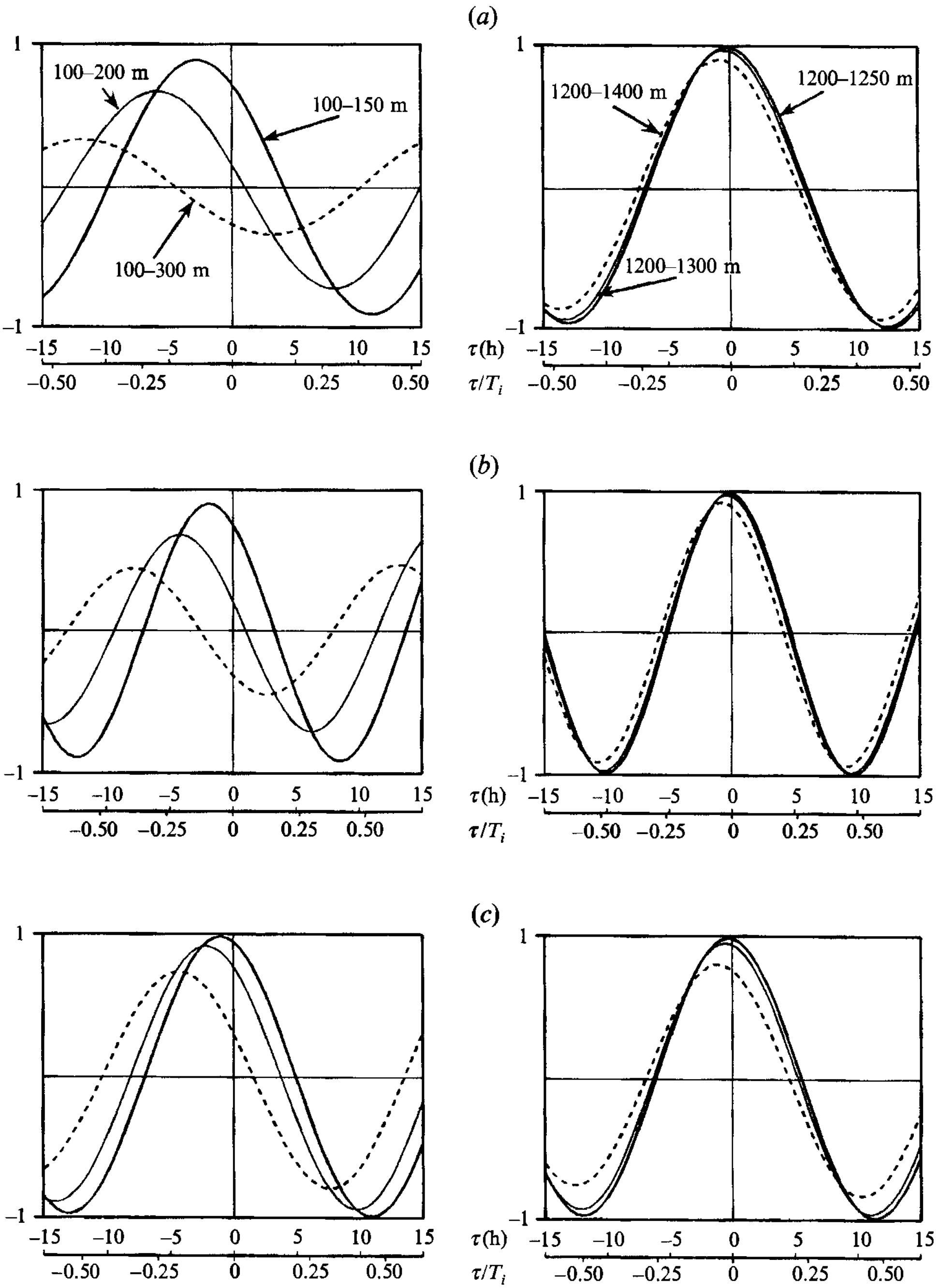

FIGURE 14. Flow due to a medium-speed front moving eastward at $U = 600$ cm/s using a variable-f model, showing the vertical correlation of u, namely $\overline{u_1(t)\,u_2(t+\tau)}/u_1^{rms}\,u_2^{rms}$. The depth pairs are indicated on the plots. The left column shows correlations in the thermocline, and the right column shows correlations at mid-depth and (*a*) $\theta = 25°$ N, (*b*) $\theta = 35°$ N, (*c*) $\theta = 30°$ N. The f is regarded as variable in (*a*) and (*b*), and as constant in (*c*). Note that the correlation is lower in the variable-f model, and in the thermocline.

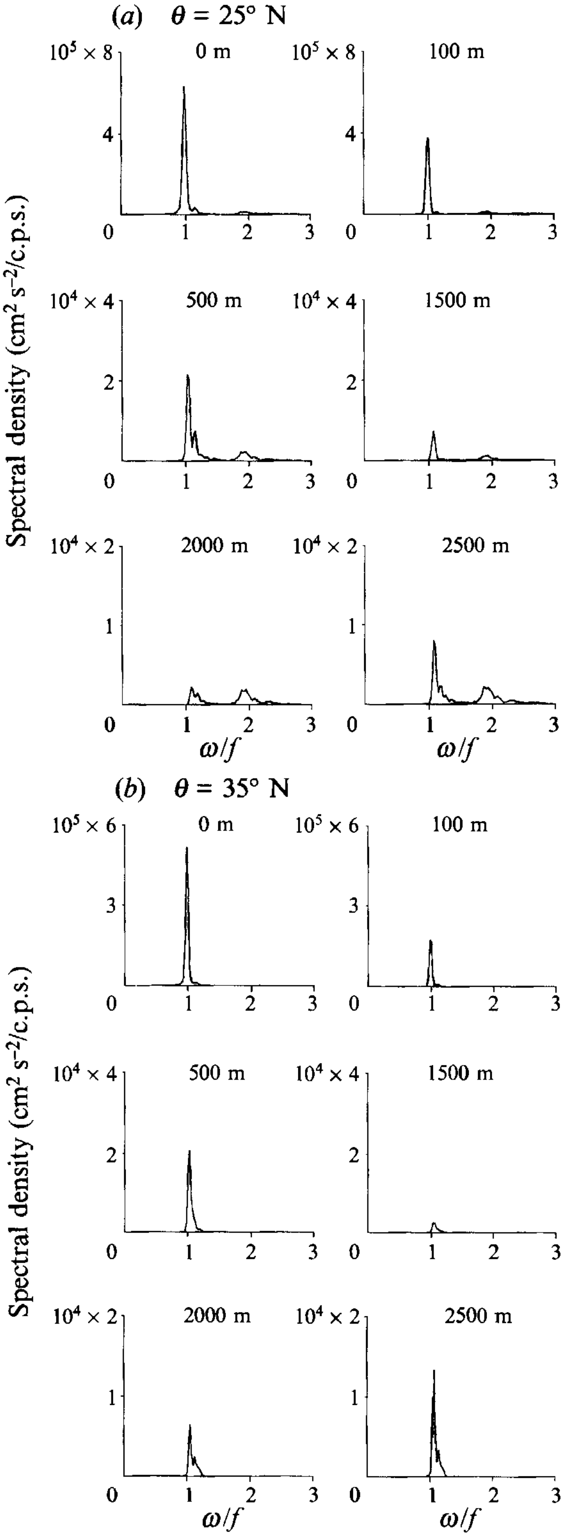

FIGURE 15. Flow due to a slow front moving eastward at $U = 300$ cm/s using a variable-f model, showing spectra of $\overline{u^2}$ at 25° N and 35° N at various depths. Vertical scales are exaggerated at larger depths. Note that the spectra at 25° N contain a wider range of frequencies than the spectra at 35° N, because the waves arriving here have been generated in a wider range of latitudes in the north.

model of Kundu & Thomson (1985). For a constant-N ocean, it is shown that the hydrostatic assumption is valid if the frequency is not much larger than $(Nf)^{\frac{1}{2}}$ (figure 3). The non-hydrostatic but constant-f case is examined first. The wake contains waves of all modes, whatever the value of U. This feature is different from the hydrostatic case where the restriction $U > c_n$ applies; the reason for the difference is that c_n is the minimum allowable phase speed in a hydrostatic model, and only for $U > c_n$ can the line $\omega = Uk$ pick out the phase speed ω/k at which the waves appear steady to an observer moving at speed U (§4.4). For $c_{n+1} < U < c_n$, the lower modes $(1,\dots,n)$ generate high-frequency internal waves in the range $(Nf)^{\frac{1}{2}} < \omega < N$, and all the higher modes generate low-frequency waves in the range $f < \omega < (Nf)^{\frac{1}{2}}$. Wind fields propagating over a wide range of slow speeds excite a few low-order modes at frequencies somewhat below the local N (figure 3*a*); this can explain the broad peak (or shoulder) and high vertical correlation observed in the seasonal thermocline at frequencies somewhat below the local N (figure 4). Desaubies (1975) and Munk (1980) explained these phenomena as due to constructive interference at the turning depth, while Levine *et al.* (1983*a, b*) speculated the high correlation as being due to the critical-layer absorption of the high modes by a mean flow.

The above argument is qualitative, because N is assumed depth-independent in the dispersion relation shown in figure 3. The non-hydrostatic modes in the presence of a thermocline are discussed in Garrett & Munk (1972). At a given frequency $\omega < N_{max}$, the solution of the non-hydrostatic eigenvalue problem determines the mode shapes for an infinity of discrete values of $k_n(\omega)$, which gives the dispersion relation. The mode shapes are oscillatory in the depth range in which $\omega < N(z)$, outside of which they decay exponentially. The resulting dispersion relation resembles figure 3 qualitatively, simply because the frequency must be less than the local value of $N(z)$. Therefore the argument offered here to explain the spectral shoulder and coherence at frequencies somewhat below the local N seem promising.

To understand the behaviour of lower-frequency waves, the response to a y-independent front moving eastward is numerically calculated in a hydrostatic model with variable f. The region of integration extends from 20° N to 40° N, and the wave field is examined for $U = 1200$, 600, and 300 cm/s. Compared to the constant-f case (figures 7 and 8), the spectral widths are now larger, especially at lower latitudes (figures 9, 12, 15) where the highest frequencies are close to the ones produced at 40° N; this of course is due to the equatorward and downward propagation of the waves (figure 11). (However, such a rule does not work for the slower propagation speed $U = 300$ cm/s, where little of the highest frequency generated at 40° N appears in the deep spectra at 25° N (figure 15). This is because the high value of the local maximum frequency, caused by a combination of wind translation and β-effect, results in a fast downward leakage from the surface layer and a domination of the local generation over equatorward propagation (§5.4).) Compared with the constant-f model, persistence of the oscillations in the surface layer is shorter, and consequently the wave amplitudes in the thermocline are larger (compare figures 8*b* and 10); the waves are also more intermittent due to the larger spectral width (figures 10, 13).

Compared to the constant-f model, the waves are vertically less correlated in the thermocline (figure 14, left column) due to the contribution of a larger bandwidth of vertical modes, each generating a different frequency ω_n. In the deep ocean, however, domination by one or two modes make the correlation high (figure 14, right column), and the waves appear as standing modes, as observed by Fu (1981). (Additional modes, which have angular velocities only slightly above f, would appear in an inviscid deep ocean if the integration were carried forward for a time much longer than 30 days. This,

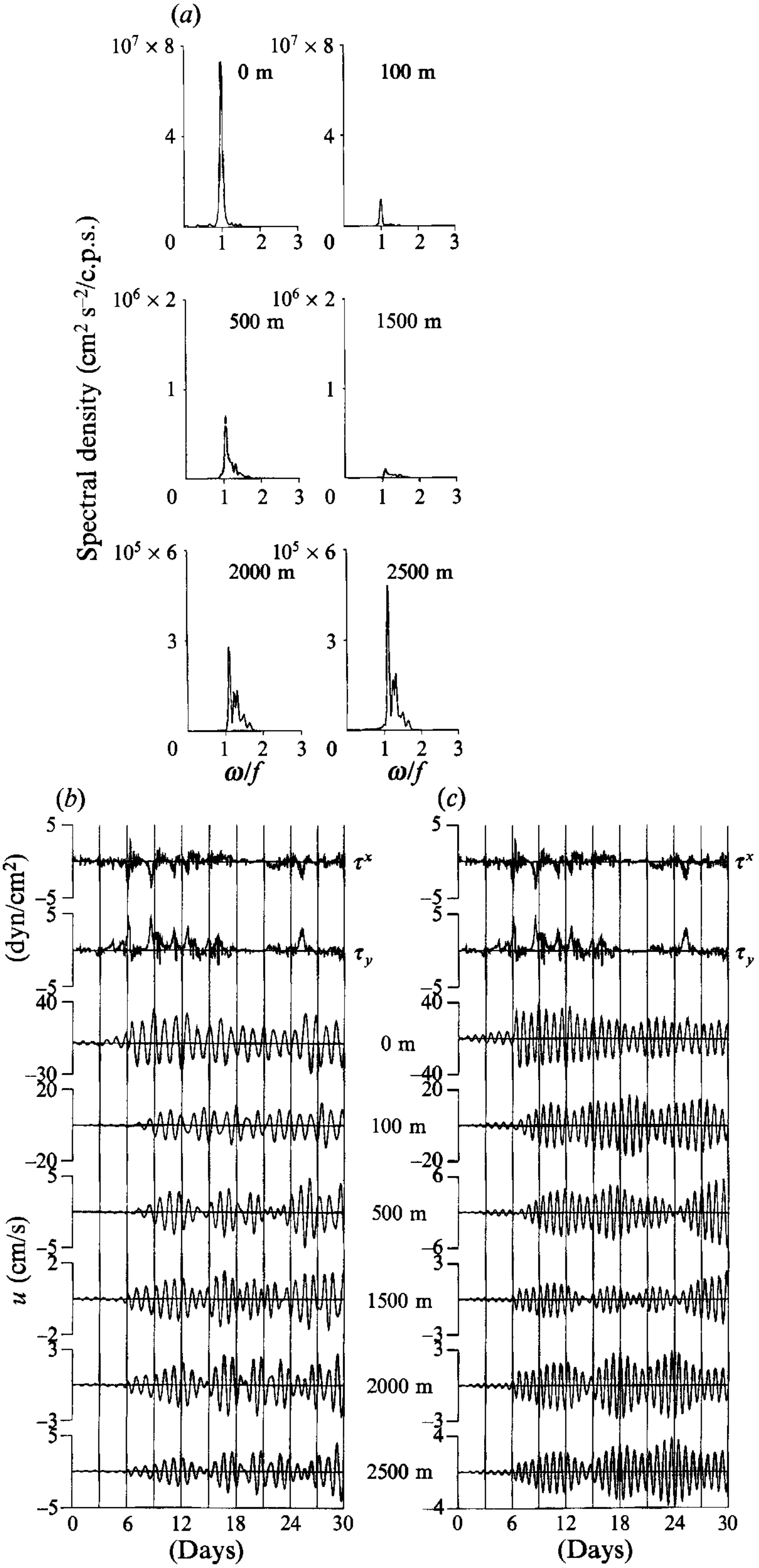

FIGURE 16(*a–c*). For caption see facing page.

of course, will not happen in the presence of some dissipation. In fact, several calculations show that the frictional decay time of inertial waves generated in the deep ocean by a single storm is likely to be several months long, but not years.) The model spectra in the deep ocean also show a larger proportion of high-frequency content (figures 9, 12, 15, 16), in agreement with the observations. Compared to the observations the vertical correlation scales seem rather high. This is presumably due to the assumed y-independence of the wind field. If some randomness is added to the y-distribution of the wind, then the equatorward and downward dispersion of waves from higher latitudes will result in a less vertical correlation at a lower latitude.

The fundamental reason for faster downward leakage of mixed-layer energy and other differences between the variable-f and constant-f models is the development of a constantly decreasing meridional wavelength $\lambda_y = 2\pi/\beta t$. Although this expression was derived by D'Asaro (1989) in a problem forced by a spatially uniform switched-on wind, the present calculations with a zonally moving meridionally structureless wind illustrate the same effect quite graphically (figure 11; also figure 5). A zonally propagating wind develops an additional wavelength λ_x, and the two effects (λ_x and λ_y) combine to result in greater horizontal inhomogeneity, and consequently a higher frequency and a faster downward penetration of energy.

Several studies (for example Pollard 1970; Smith 1973) noted that their models cannot account for the low persistence of inertial energy in the surface layer, and suggested that the effect may be due to wind stress destroying as well as creating inertial oscillations. While this may be true for particular isolated events, it cannot be a general principle. On the average the random appearance of wind events should increase the inertial amplitudes as $t^{\frac{1}{2}}$, like in a random walk (see figure 1 of Kundu 1984). The fact that the wave amplitudes in the surface layer forced by an observed wind stress containing 'random' events of realistic magnitude do not increase in the present calculations (figure 16) is due to the fast downward leakage caused by the dual effects of wind translation and β. Figure 16 also shows that on average the amplitude in the deep ocean does increase, perhaps as $t^{\frac{1}{2}}$, due to random superposition of energy leaking out of the surface layer. In a month the maximum amplitudes near the bottom reach values of order 4 cm/s, in agreement with several observations by Sanford and his group.

The two important aspects left out of the present calculations are the influence of a background mean (or low-frequency) flow, and nonlinearity. Kunze (1985) and Kunze & Sanford (1986) discuss how the mean flow can cause such effects as smearing out of the spectral peaks by Doppler effect, changing the effective inertial frequency to $f_{eff} = f + \frac{1}{2}\zeta$ (where ζ is the vorticity of the background flow), trapping the energy in regions of negative vorticity, and critical-layer absorption. The model spectra (figure 16*a*) due to a realistic forcing are too spiky, and almost certainly they will be smoothed out due to nonlinear energy cascade and interaction with the mean flow, possibly ending with the ω^{-2} form of Garret–Munk (figure 4*a*).

FIGURE 16. Flow due to a wind series measured at a fixed point off the coast of British Columbia, assumed frozen and propagating at $U = 600$ cm/s, using a variable-f model. In (*a*) the spectra of $\overline{u^2}$ at 25° N are shown, and in (*b*) and (*c*) time series of wind stress and u at different depths at 25° N and 35° N respectively are shown. As expected the spectra have a large high-frequency content at 25° N, and the time series reflect this. In contrast, the spectra at 35° N (not shown) had a much smaller bandwidth, which is also reflected in the time series. Note that the amplitude reaches values of around 4 cm/s in the deep ocean.

This research was funded by NSF Grant No. OCE-9103152. I thank Eric D'Asaro, Charles Eriksen, Chris Garrett, Richard Greatbatch, Murray Levine, Julian McCreary, and Robert Pinkel for helpful discussions. Rick Thomson provided the wind data, and Robert Pinkel provided a copy of figure 4(*b*). I am most grateful to Julian McCreary for giving valuable comments on the manuscript. Kevin Kohler's computer programming and drafting of figures were indispensable.

REFERENCES

ANDERSON, D. L. T. & GILL, A. 1979 Beta dispersion of inertial waves. *J. Geophys. Res.* **84**, 1836–1842.

CAIRNS, J. L. & WILLIAMS, G. O. 1976 Internal wave observations from a mid-water float. Part 2. *J. Geophys. Res.* **81**, 1943–1950.

CORNISH, C. R. & LARSEN, M. F. 1989 Observations of low-frequency waves in the lower stratosphere over Arecibo. *J. Atmos. Sci.* **46**, 2428–2439.

D'ASARO, E. A. 1985 The energy flux from the wind to near-inertial motions in the surface mixed layer. *J. Phys. Oceanogr.* **15**, 1043–1959.

D'ASARO, E. A. 1989 The decay of wind-forced mixed layer inertial oscillations due to the β effect. *J. Geophys. Res.* **94**, 2045–2056.

DESAUBIES, Y. J. F. 1975 A linear theory of internal wave spectra and coherences near Väisälä frequency. *J. Geophys. Res.* **80**, 895–899.

ERIKSEN, C. C. 1988*a* On wind forcing and observed wavenumber spectra. *J. Geophys. Res.* **93**, 4985–4992.

ERIKSEN, C. C. 1988*b* Variability in the upper-ocean internal wave field at a Sargasso sea site. *J. Phys. Oceanogr.* **18**, 1495–1513.

ERIKSEN, C. C. 1993 Equatorial ocean response to rapidly translating wind bursts. *J. Phys. Oceanogr.* **23**, 1208–1230.

FENNEL, W. & LASS, H. U. 1989 *Analytical Theory of Forced Oceanic Waves*. Berlin: Akademie.

FU, L. L. 1981 Observations and models of inertial waves in the deep ocean. *Rev. Geophys. Space Phys.* **19**, 141–170.

GARRETT, C. J. R. & MUNK, W. H. 1972 Space-time scales of internal waves. *Geophys. Fluid Dyn.* **2**, 225–264.

GARRETT, C. J. R. & MUNK, W. H. 1979 Internal waves in the ocean. *Ann. Rev. Fluid Mech.* **11**, 339–369.

GEISLER, J. E. 1970 Linear theory of the response of a two-layer ocean to a moving hurricane. *Geophys. Fluid Dyn.* **1**, 249–272.

GEISLER, J. E. & DICKINSON, R. E. 1972 The role of variable Coriolis parameter in the propagation of inertia-gravity waves during the geostrophic adjustment. *J. Phys. Oceanogr.* **2**, 263–272.

GILL, A. E. 1982 *Atmosphere-Ocean Dynamics*. Academic.

GILL, A. E. 1984 On the behavior of internal waves in the wakes of storms. *J. Phys. Oceanogr.* **14**, 1129–1151.

GOULD, W. J., SCHMITZ, W. J. & WUNCH, C. 1974 Preliminary field results for a Mid-Ocean Dynamics Experiment (MODE-0). *Deep-Sea Res.* **21**, 911–932.

GREATBATCH, R. J. 1983 On the response of the ocean to a moving storm: The nonlinear dynamics. *J. Phys. Oceanogr.* **13**, 357–367.

GREATBACH, R. J. 1984 On the response of the ocean to a moving storm: parameters and scales. *J. Phys. Oceanogr.* **14**, 59–78.

KUNDU, P. K. 1976 An analysis of inertial oscillations observed near Oregon coast. *J. Phys. Oceanogr.* **6**, 879–893.

KUNDU, P. K. 1984 Generation of coastal inertial oscillations by time-varying wind. *J. Phys. Oceanogr.* **14**, 1901–1913.

KUNDU, P. K. 1986 A two-dimensional model of inertial oscillations generated by a propagating wind field. *J. Phys. Oceanogr.* **16**, 1399–1411.

KUNDU, P. K. 1990 *Fluid Mechanics*. Academic.

KUNDU, P. K. & THOMSON, R. E. 1985 Inertial oscillations due to a moving front. *J. Phys. Oceanogr.* **15**, 1076–1084 (referred to herein as KT85).

KUNZE, E. 1985 Near-inertial wave propagation in geostrophic shear. *J. Phys. Oceanogr.* **15**, 544–565.

KUNZE, E. & SANFORD, T. B. 1986 Near-inertial wave interactions with mean flow and bottom topography near Caryn seamount. *J. Phys. Oceanogr.* **16**, 109–120.

LEVINE, M. D., PAULSON, C. A., BRISCOE, M. G., WELLER, R. A. & PETERS, H. 1983*a* Internal waves in JASIN. *Phil. Trans. R. Soc. Lond.* A **308**, 389–405.

LEVINE, M. D., SZOEKE, R. A. DE & NIILER, P. P. 1983*b* Internal waves in the upper ocean during MILE. *J. Phys. Oceanogr.* **13**, 240–257.

MCCOMAS, C. H. & BRETHERTON, F. P. 1977 Resonant interaction of oceanic internal waves. *J. Geophys. Res.* **82** 1397–1412.

MCCREARY, J. P. 1981 A linear stratified ocean model of the equatorial undercurrent. *Phil. Trans. R. Soc. Lond.* A **298**, 603–635.

MUNK, W. H. 1980 Internal wave spectra at the buoyant and inertial frequencies. *J. Phys. Oceanogr.* **10**, 1718–1728.

MUNK, W. H. 1981 Internal waves. In *Evolution of Physical Oceanography* (ed. B. A. Warren & C. Wunch), p. 623. MIT Press.

MUNK, W. H. & PHILLIPS, N. 1968 Coherence and band structure of inertial motion in the sea. *Rev. Geophys. Space Phys.* **6**, 447–472.

OLBERS, D. 1983 Internal gravity waves. In *Oceanography*, vol. 3 (ed. J. Sündermann). Springer.

ORLANSKI, I. 1976 A simple boundary condition for unbounded hyperbolic flows. *J. Comput. Phys.* **21**, 251–269.

PADUAN, J. D., SZOEKE, R. A. DE & WELLER, R. A. 1989 Inertial oscillations in the upper ocean during the Mixed Layer Experiment. *J. Geophys. Res.* **94**, 4835–4842.

PHILLIPS, O. M. 1977 *The Dynamics of the Upper Ocean*. Cambridge University Press.

PINKEL, R. 1975 Upper ocean internal wave observations from FLIP. *J. Geophys. Res.* **80**, 3892–3910.

PINKEL, R. 1981 Observations of the near-surface internal wavefield. *J. Phys. Oceanogr.* **11**, 1248–1257.

PINKEL, R. 1985 A wavenumber-frequency spectrum of upper ocean shear. *J. Phys. Oceanogr.* **15**, 1453–1469.

POLLARD, R. T. 1970 On the generation by winds of inertial waves in the ocean. *Deep-Sea Res.* **17**, 795–812.

PRICE, J. F. 1983 Internal wave wake of a moving storm. Part I: Scales, energy budget and observations. *J. Phys. Oceanogr.* **13**, 949–965.

SANFORD, T. B. 1975 Observations of the vertical structure of internal waves. *J. Geophys. Res.* **80**, 3861–3871.

SHEN, C. Y. & HOLLOWAY, G. 1986 A numerical study of the frequency and the energetics of nonlinear internal gravity waves. *J. Geophys. Res.* **91**, 953–973.

SMITH, R. 1973 Evolution of inertial frequency oscillations. *J. Fluid Mech.* **60**, 383–389.

THOMSON, R. E. & HUGGETT, W. S. 1981 Wind-driven inertial oscillations of large spatial coherence. *Atmos. Ocean.* **19**, 281–306.

THORPE, S. A. 1975 The excitation, dissipation, and interaction of internal waves in the open ocean. *J. Geophys. Res.* **80**, 328–338.

WUNCH, C. & GILL, A. E. 1976 Observations of equatorially trapped waves in Pacific sea level variations. *Deep-Sea Res.* **23**, 371–390.